



Nonlinear vibration analysis in precision motion stage with PID and time-delayed feedback controls

Sunit Kumar Gupta · Jiamin Wang ·
Oumar R. Barry 

Received: 1 January 2020 / Accepted: 19 June 2020
© Springer Nature B.V. 2020

Abstract We investigate the control of friction-induced vibration in a precision motion stage under the effect of the LuGre friction dynamics. We consider a lumped parameter model of the precision motion stage with PID and linear time-delayed state feedback control acting in the direction of the motion of the stage. Linear stability analysis reveals the criticality of integral gain in the stability and, accordingly, the existence of multiple stability lobes and codimension-2 Hopf points for a given choice of system parameters. The nature of the bifurcation is determined by an analytical study using the method of multiple scales and harmonic balance. We observe the existence of both subcritical and supercritical Hopf bifurcations in the system, depending on the choice of control parameters. Hence, the nonlinearity due to dynamic friction model could both be stabilizing or destabilizing in nature, and therefore, stick-slip nonlinearity is essential to capture the global behavior of the system dynamics. Furthermore, numerical bifurcation analysis of the system reveals the existence of period-doubling bifurcation near the Hopf points. We observe complicated solutions such as period-4, quasi-periodic, large-amplitude stick-slip limit cycles along with chaotic attractor in the system.

Keywords Precision motion stage · Method of multiple scales · Subcritical and supercritical

S. K. Gupta · J. Wang · O. R. Barry (✉)
Department of Mechanical Engineering, Virginia Tech,
Blacksburg, VA 24061, USA
e-mail: obarry@vt.edu

bifurcation · Period-doubling bifurcation · Chaotic attractor

1 Introduction

In machining, additive manufacturing, and semiconductor fabrication industries, motion stages are intensively used for the precision positioning at macro- and nano-levels [1–4]. These precision motion stages can be broadly classified into four different categories: (1) flexural-based, (2) magnetic-based, (3) fluidic-based, and (4) mechanical bearing-based [1, 5–7]. Mechanical bearing-based motion stages (MBMS) (e.g., sliding and rolling bearings) are more popular as compared to others in the industrial applications due to their large motion range, high off-axis stiffness, and cost-effectiveness [7]. However, one of the phenomena afflicting the motion of MBMS is precession or static friction between the rolling bearing elements and rigid supporting surface as the motion stage transits from rest to full motion. This precession friction adversely affects the positioning precision, speed, long settling times, stick-slip phenomena, and further causing large tracking errors [8–14]. The commonly applied controller in the motion stage to control the motion of MBMS includes one or a combination of proportional (P), integral (I), and derivative (D) terms [10, 15, 16]. On the other hand, implementing feedback controllers leads to self-excited limit cycles due to friction, also referred to as friction-induced vibration [11], resulting in fur-

ther control performance deterioration. Therefore, to enhance the performance of precision motion stages, it is necessary to have a complete understanding of the dynamics of the precision motion stage based on the different values of control parameters.

Different methods can be used to control frictional systems and suppress self-excited friction-induced vibrations. These methods can be broadly classified into three categories: (1) application of advanced controllers (adaptive controller, model predictive controller) [17–20] (2) passive suppression of vibrations through friction isolators or compliant joints method [21, 22], and (3) the use of time-delayed feedback controllers [23–30]. A common problem of implementing advanced controllers is related to algorithm complexity determined by the structural model, which may lead to unsatisfactory performance at high-frequency controls due to hardware limitation [31, 32]. Vibration suppression realized by mechanical enhancements can be limited by the practical range of design parameters. Mechanical add-ons may also introduce additional coupling of dynamics, i.e., in the case of friction isolator, the stability range of control gain selection is reduced by multiple factors including the mass ratio and the stiffness/damper [33, 34].

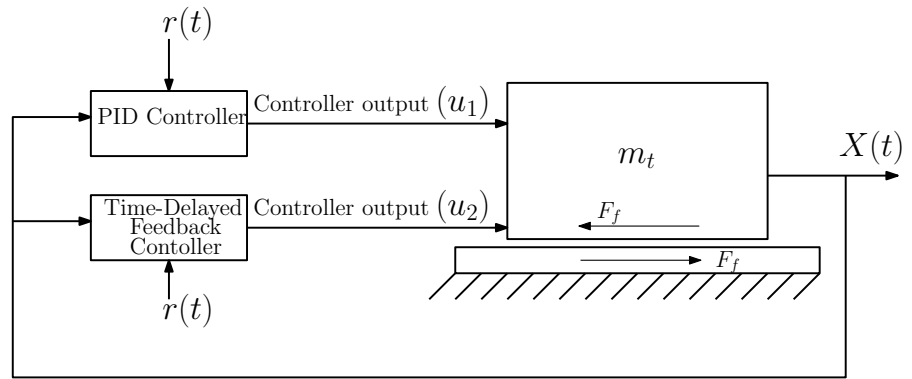
In recent years, the use of time-delayed feedback control has become prevalent to control vibration in complex systems. For the sake of completeness, we summarize some of the pioneering works here. In 2003, Maccari [23] successfully implemented time-delayed state feedback to control the vibration of a cantilever beam for the case of primary resonance and observed reduction in the amplitude peaks. Later on, Atay [24] and Maccari [25] studied the control of free, forced, and parametric excitation of a van der Pol oscillator using time-delayed feedback control. Hu et al. [26] investigated the primary and subharmonic resonance of a forced Duffing oscillator with time-delayed state feedback. Qian and Tang [27] used a time-delayed feedback controller to stabilize the vibration of a nonlinear beam under moving load. Following these studies, time-delayed feedback controllers are also successfully implemented for the control of self-excited friction-induced vibrations. Das and Mallik [28] were the first ones to study time-delayed PD feedback control to suppress self-excited vibration in friction-driven systems. Chatterjee [29] studied the control of different types of friction-induced instabilities using time-delayed feedback. Neubauer et al. [30] investigated analytically and

experimentally the use of time-delayed feedback control to quench stick-slip vibrations in an automotive disc brake.

One of the crucial steps in modeling friction-induced vibrations is the choice of the friction model. From experimental investigations, it was observed that static friction laws do not capture the complete dynamical effects of friction-induced vibrations such as presliding, change in friction with time, and relative velocity. Therefore, dynamics friction model are required to understand these dynamical effects. One of the popular dynamic friction models is the LuGre friction model [35], which includes viscous friction, pre-motion friction (presliding/prerolling), and hysteresis effects together and, hence, has been considered in the current analysis. Nevertheless, the nonlinear analysis of friction-induced vibration with the LuGre friction model revealed the nature of the bifurcation is subcritical, which further causes the loss of global stability of equilibrium points near the stability boundaries [36]. However, it has been observed that with the proper choice of control parameters in time-delayed feedback controllers the nature of bifurcation can be changed from subcritical to supercritical, and hence, global stability of equilibrium points near the stability boundaries can be achieved.

We emphasize that although the use of time-delayed feedback control to quench friction-induced vibration is well-established in the literature, it has not been implemented to control friction-induced vibration in PID-controlled motion stages. Therefore, this work is believed to be the first study to examine this problem, in which we use a linear time-delayed feedback controller in a PID-controlled motion stage. We use linear time-delayed feedback to control the friction-induced vibrations in a motion stage under the effect of the LuGre friction model. It has been observed that for a given set of control parameters in PID, the nature of bifurcation can be changed with the help of a time-delayed feedback controller. The rest of the paper is organized as follows. In Sect. 2, we present the complete mathematical model of MBMS. It also includes a brief description of the LuGre model, along with the nondimensionalization of the governing equation of motions. Linear stability analysis and, accordingly, the analytical forms of the Hopf points are presented in Sect. 3. In Sect. 4, a detailed analytical nonlinear analysis of the system is presented using the method of multiple scales and harmonic balance. Results from linear and nonlinear

Fig. 1 Schematic of precision motion stage with PID and time-delayed feedback controller



analysis along with numerical bifurcation analysis is presented in Sect. 5. In Sect. 6, some conclusions are drawn from the findings of the analysis.

2 The mathematical model of a MBMS with dynamic (LuGre) friction model

In this section, we briefly outline the mathematical model used for the analysis in the current study. We model the precision motion stage as a single degree of freedom system, which is in frictional contact with the rigid surface since the rail of the mechanical bearing is fixed to the ground. Also, we consider this model with control forces applied along the direction of the motion of the stage only. The physical model of the system is shown in Fig. 1, in which u_1 and u_2 are the feedback control forces corresponding to PID and time-delayed controllers, respectively. m_t is the mass of motion stage, F_f is the frictional force between the motion stage and rigid surface, $r(t)$ is the setpoint/reference signal, and $X(t)$ is the motion of the stage.

Therefore, the equation governing the motion of the stage can be written as

$$m_t \ddot{X} = u_1 + u_2 - F_f, \tag{1}$$

where the PID and time-delayed controller force (u_1 and u_2) can be calculated as

$$u_1 = -k_p^* \alpha - k_d^* \dot{\alpha} - k_i^* \int \alpha dt, \tag{2}$$

and

$$u_2 = K_0^* (\alpha(t - T^*) - \alpha(t)). \tag{3}$$

In the above expressions of u_1 and u_2 , k_p^* , k_d^* , and k_i^* represent the proportional, differential, and integral gains, respectively, K_0^* represents the delay gain, T^*

represents the time delay, and α represents the tracking error. The tracking error can be expressed in terms of the motion of the stage, $X(t)$, and the reference signal, $r(t)$, as

$$\alpha = X(t) - r(t). \tag{4}$$

On substituting the expressions for control forces (Eqs. 2, 3) in equation of motion (Eq. 1) and writing in terms of tracking error α , we get

$$m_t \ddot{\alpha} + k_d^* \dot{\alpha} + k_p^* \alpha + k_i^* \int \alpha dt = K_0^* (\alpha(t - T^*) - \alpha(t)) - F_f + m_t \ddot{r}. \tag{5}$$

The next step in the mathematical modeling is the selection of the dynamical friction model. The LuGre friction model incorporates viscous friction, premotion friction (presliding/prerolling), and hysteresis effects together and, hence, is widely used in the analysis of real-life dynamical friction problems [35,37–39]. One of the essential characteristics of the LuGre friction model is that unlike other friction models, the LuGre friction model does not only depend on the relative velocity but also on the internal state variable. Also, the evolution of this internal state variable with time is governed by a differential equation. Therefore, instead of resulting in a unique value of the friction force for a given relative velocity during acceleration and deceleration, it can give different values of friction force in these two phases depending on the evolution of the internal state variable.

The LuGre friction model incorporates microscopic degrees of freedom by modeling asperities of the contact surfaces as elastic spring-like bristles with damping (as shown in Fig. 2). Therefore, the total friction force can be represented as the sum of the forces developed from the deflection of the bristles and the macroscopic

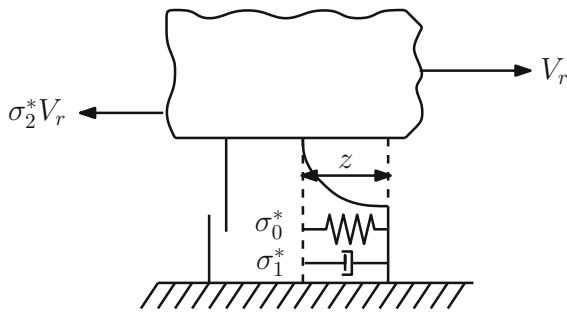


Fig. 2 Schematic of the friction dynamics between the contact surfaces

viscous friction, which is proportional to the relative velocity between contacting surfaces. Therefore, if z represents the average bristle deflection, which also represents the internal state variable, the friction force in the LuGre model can be defined as [35]:

$$F_f = \sigma_0^* z + \sigma_1^* \dot{z} + \sigma_2^* V_r, \tag{6}$$

where σ_0^* and σ_1^* are the contact stiffness the micro-damping of the bristle, respectively, σ_2^* is the macroscopic viscous friction between the contact surfaces, and $V_r = \dot{X} = \dot{\alpha} + \dot{r}$ is the relative velocity between the two moving surfaces. Also, the evolution of the average bristle deflection z with time is governed by [35,40]:

$$\dot{z} = V_r - \frac{\sigma_0^* |V_r|}{g(V_r)} z = V_r \left(1 - \frac{\sigma_0^* \text{sgn}(V_r)}{g(V_r)} z \right), \tag{7}$$

where $g(V_r) > 0$ describes the Stribeck effect. To capture dropping characteristic, Wit et al. [35] suggested the use of Gaussian function model for $g(V_r)$ in the form of :

$$g(V_r) = f_C^* + (f_S^* - f_C^*) e^{-(V_r/V_s)^2}, \tag{8}$$

where f_C^* is the Coulomb friction, f_S^* is the static friction, and V_s is the Stribeck velocity threshold. However, the limitations of this model have been observed in the analytical analysis of the system [40,41]. To overcome this shortcoming, the positive-valued function $g(V_r)$ was modified and represented by an exponential function [40,41]:

$$g(V_r) = f_C^* + (f_S^* - f_C^*) e^{-\tilde{a}|V_r|}, \tag{9}$$

where \tilde{a} is the slope parameter. Having defined the dynamical frictional model, we note that Eqs. (5), (6), (7), and (9) together govern the complete dynamics of the system. Further, we introduce the following non-dimensional scales and parameters:

$$\begin{aligned} x &= \frac{\alpha}{X_0}, \quad \tilde{z} = \frac{z}{X_0}, \quad X_0 = \frac{g}{\omega_0^2}, \quad \omega_0 = \sqrt{\frac{k_p^*}{m_t}}, \\ \tau &= \omega_0 t, \quad \zeta = \frac{k_d^*}{2m_t \omega_0}, \quad k_i = \frac{k_i^*}{m_t \omega_0^3}, \\ T &= \omega_0 T^*, \quad K_0 = \frac{K_0^*}{m_t \omega_0^2}, \quad v_r = \frac{V_r}{X_0 \omega_0}, \\ \sigma_0 &= \frac{\sigma_0^*}{m_t \omega_0^2}, \quad \sigma_1 = \frac{\sigma_1^*}{m_t \omega_0}, \quad \sigma_2 = \frac{\sigma_2^*}{m_t \omega_0}, \\ f_c &= \frac{f_c^*}{m_t X_0 \omega_0^2}, \quad f_s = \frac{f_s^*}{m_t X_0 \omega_0^2}, \quad a = \tilde{a} \omega_0 X_0. \end{aligned} \tag{10}$$

Using above-mentioned non-dimensional scales and parameters and assuming constant reference velocity ($\dot{r} = 0$), the governing equations of motion can be non-dimensionalized as

$$\begin{aligned} \ddot{x} + 2\zeta \dot{x} + x + k_i \int x d\tau &= K_0 (x(\tau - T) - x(\tau)) \\ &\quad - \left(\sigma_0 \tilde{z} + \sigma_1 v_r \left(1 - \frac{\sigma_0 \text{sgn}(v_r)}{g(v_r)} \tilde{z} \right) + \sigma_2 v_r \right), \end{aligned} \tag{11a}$$

$$\dot{\tilde{z}} = v_r \left(1 - \frac{\sigma_0 \text{sgn}(v_r)}{g(v_r)} \tilde{z} \right). \tag{11b}$$

In the above governing equations, overhead dot ($\dot{\cdot}$) represents the derivative with respect to the non-dimensional time τ . For the sake of simplicity in the analytical treatment of governing equations, we rewrite Eq. (11) compactly in state-space form as:

$$\dot{x}_1 = x_2, \tag{12a}$$

$$\begin{aligned} \dot{x}_2 &= -2\zeta x_2 - x_1 - k_i x_3 + K_0 (x_1(\tau - T) - x_1) \\ &\quad - \left(\sigma_0 x_4 + \sigma_1 v_r \left(1 - \frac{\sigma_0 x_4}{g(v_r)} \text{sgn}(v_r) \right) + \sigma_2 v_r \right), \end{aligned} \tag{12b}$$

$$\dot{x}_3 = x_1, \tag{12c}$$

$$\dot{x}_4 = v_r \left(1 - \frac{\sigma_0 x_4}{g(v_r)} \text{sgn}(v_r) \right), \tag{12d}$$

where $[x_1, x_2, x_3, x_4] = [x(\tau), \dot{x}(\tau), \int x d\tau, \tilde{z}(\tau)]$. Therefore, if v_{rv} represents the non-dimensional constant reference velocity, the non-dimensional relative velocity, v_r , can be written as

$$v_r = \dot{x} + v_{rv} = x_2 + v_{rv}.$$

Expanding $\frac{1}{g(v_r)} = \frac{1}{g(v_{rv} + x_2)}$ in a Taylor series for small amplitude of x_2 and keeping terms till third order, we get

$$\frac{1}{g(v_{rv} + x_2)} = g_0 + g_1x_2 + g_2x_2^2 + g_3x_2^3. \tag{13}$$

In the above expansion of $1/g(v_r)$, g_i are given by

$$\begin{aligned} g_0 &= \frac{1}{g(v_{rv})} = \frac{1}{g}, \quad g_1 = -\frac{1}{g^2} \frac{\partial g}{\partial v_{rv}}, \\ g_2 &= \frac{1}{g^3} \left[\left(\frac{\partial g}{\partial v_{rv}} \right)^2 - \frac{g}{2} \frac{\partial^2 g}{\partial v_{rv}^2} \right], \\ g_3 &= -\frac{1}{g^4} \left[\left(\frac{\partial g}{\partial v_{rv}} \right)^3 - g \frac{\partial g}{\partial v_{rv}} \frac{\partial^2 g}{\partial v_{rv}^2} + \frac{g^2}{6} \frac{\partial^3 g}{\partial v_{rv}^3} \right]. \end{aligned} \tag{14}$$

On substituting Eq. (13) in Eq. (12) and simplifying terms for pure slipping motion, i.e., $v_r > 0$ (which further implies $\text{sgn}(v_r) = 1$), we get

$$\dot{x}_1 = x_2, \tag{15a}$$

$$\begin{aligned} \dot{x}_2 &= -(K_0 + 1)x_1 - k_i x_3 \\ &\quad + \left(\sigma_1 \sigma_0 g_3 x_2^4 \right. \\ &\quad + (\sigma_1 \sigma_0 g_0 + \sigma_1 v_{rv} \sigma_0 g_1) x_2 \\ &\quad + (\sigma_1 v_{rv} \sigma_0 g_2 + \sigma_1 \sigma_0 g_1) x_2^2 \\ &\quad - \sigma_0 + \sigma_1 v_{rv} \sigma_0 g_0 \\ &\quad + (\sigma_1 \sigma_0 g_2 + \sigma_1 v_{rv} \sigma_0 g_3) x_2^3 \left. \right) x_4(t) \\ &\quad + K_0 x_1 (\tau - T) - \sigma_1 v_{rv} \\ &\quad + (-2\zeta - \sigma_2 - \sigma_1) x_2 - \sigma_2 v_{rv}, \end{aligned} \tag{15b}$$

$$\dot{x}_3 = x_1, \tag{15c}$$

$$\begin{aligned} \dot{x}_4 &= \left(-\sigma_0 g_3 x_2^4 - (v_{rv} \sigma_0 g_2 + \sigma_0 g_1) x_2^2 \right. \\ &\quad - (v_{rv} \sigma_0 g_1 + \sigma_0 g_0) x_2 \\ &\quad - (\sigma_0 g_2 + v_{rv} \sigma_0 g_3) x_2^3 - v_{rv} \sigma_0 g_0 \left. \right) x_4 \\ &\quad + x_2 + v_{rv}. \end{aligned} \tag{15d}$$

The steady states of Eq. (15) can be obtained by setting derivatives of states as 0, i.e., $\dot{x}_1 = \dot{x}_2 = \dot{x}_3 = \dot{x}_4 = 0$ to obtain

$$\begin{aligned} x_{1s} &= 0, \quad x_{2s} = 0, \quad x_{3s} = -\frac{g_0 \sigma_2 v_{rv} + 1}{g_0 k_i}, \\ x_{4s} &= \frac{1}{\sigma_0 g_0}. \end{aligned} \tag{16}$$

For the analytical treatment of the governing equations, we introduce a small parameter ϵ , ($\epsilon \ll 1$) in the equations by shifting the origin of the solution to the equilibrium state as

$$x_i(t) = x_{is} + \epsilon y_i(t), \quad \text{for } i = 1, 2, 3, 4 \tag{17}$$

where $y_i(t)$ s are shifted coordinates. Thus, the governing equations of motion in shifted coordinates can be written as

$$\dot{y}_1 = y_2, \tag{18a}$$

$$\begin{aligned} \dot{y}_2 &= K_0 y_1 (\tau - T) - (1 + K_0) y_1 - h_1 y_2 - k_i y_3 \\ &\quad - h_2 y_4 + \epsilon \left(h_0 \sigma_1 h_3 y_2^2 + \sigma_1 h_4 y_2 y_4 \right) \\ &\quad + \epsilon^2 \left(\sigma_1 h_5 y_2^3 + \sigma_0 \sigma_1 h_3 y_4 y_2^3 \right) + \mathcal{O}(\epsilon^3), \end{aligned} \tag{18b}$$

$$\dot{y}_3 = y_1, \tag{18c}$$

$$\begin{aligned} \dot{y}_4 &= -v_{rv} g_1 h_0 y_2 - v_{rv} \sigma_0 g_0 y_4 \\ &\quad - \epsilon \left(h_0 h_3 y_2^2 + h_4 y_2 y_4 \right) \\ &\quad - \epsilon^2 \left(h_5 y_3^3 + \sigma_0 h_3 y_2^2 y_4 \right) + \mathcal{O}(\epsilon^3). \end{aligned} \tag{18d}$$

where $h_0 = \frac{1}{g_0}$, $h_1 = \sigma_2 - h_0 \sigma_1 v_{rv} g_1 + 2\zeta$, $h_2 = \sigma_0 (1 - \sigma_1 v_{rv} g_0)$, $h_3 = (v_{rv} g_2 + g_1)$, $h_4 = \sigma_0 (g_0 + v_{rv} g_1)$, and $h_5 = h_0 (g_2 + v_{rv} g_3)$. Note that, we have already divided the expanded equation throughout by ϵ , to get the above perturbed delay differential equation (DDE). From the above equations, we can observe that all the nonlinear terms are appearing at higher order of ϵ , and the unperturbed linear DDE can be obtained by setting $\epsilon = 0$. In the next section, we present the linear stability analysis to obtain the values of control parameters for the stable equilibrium.

3 Linear stability analysis

In this section, the linear stability analysis of our system (Eq. 18) is presented and, accordingly, the stability regime in the space of control parameters (k_i , ζ , K_0 , and T) is obtained. Note that this linear analysis plays an important role in the nonlinear analysis of the system as it provides the solution to the unperturbed linear equation, which will be further used to construct the solution for perturbed nonlinear equation Eq. (18). The linearized coupled system of the equation can be obtained by setting $\epsilon = 0$ in Eq. (18) to obtain

$$\dot{y}_1 = y_2, \tag{19a}$$

$$\begin{aligned} \dot{y}_2 &= K_0 y_1 (\tau - T) - (1 + K_0) y_1 \\ &\quad - h_1 y_2 - k_i y_3 - h_2 y_4, \end{aligned} \tag{19b}$$

$$\dot{y}_3 = y_1, \tag{19c}$$

$$\dot{y}_4 = -v_{rv} g_1 h_0 y_2 - v_{rv} \sigma_0 g_0 y_4. \tag{19d}$$

To obtain the characteristic equation, we assume $y_1, y_2, y_3,$ and y_4 are synchronous with each other, and accordingly, we set

$$\begin{pmatrix} y_1(\tau) \\ y_2(\tau) \\ y_3(\tau) \\ y_4(\tau) \end{pmatrix} = \begin{pmatrix} y_{10} \\ y_{20} \\ y_{30} \\ y_{40} \end{pmatrix} e^{\lambda\tau}, \tag{20}$$

into Eq. (19) and get

$$y_{10}\lambda - y_{20} = 0, \tag{21a}$$

$$\begin{aligned} (1 + K_0 - K_0 e^{-\lambda T}) y_{10} + (\lambda + h_1) y_{20} \\ + k_i y_{30} + h_2 y_{40} = 0, \end{aligned} \tag{21b}$$

$$y_{30}\lambda - y_{10} = 0, \tag{21c}$$

$$v_{rv} g_1 h_0 y_{20} + (\lambda + v_{rv} \sigma_0 g_0) y_{40} = 0. \tag{21d}$$

$$K_{0,cr} = \frac{\omega^8 + (a_1^2 - 2a_2)\omega^6 + (-2v_{rv}\sigma_0g_0a_1 + a_2^2 + 2k_iv_{rv}\sigma_0g_0 - 2k_ia_1)\omega^4 + (v_{rv}^2\sigma_0^2g_0^2 + 2k_iv_{rv}\sigma_0g_0 + k_i^2 - 2k_iv_{rv}\sigma_0g_0a_2)\omega^2 + g_0^2\sigma_0^2v_{rv}^2k_i^2}{\omega^6 + (v_{rv}\sigma_0g_0a_1 - a_2)\omega^4 - \omega^2v_{rv}^2\sigma_0^2g_0^2} \tag{24}$$

For the nontrivial solution of y_{i0} (for $i = 1, 2, 3, 4$), the determinant of the coefficient matrix of Eq. (21) must vanish. This solvability condition further leads to the characteristic equation as

$$\begin{aligned} \lambda^4 + a_1\lambda^3 + (a_2 + K_0 - K_0 e^{-\lambda T})\lambda^2 \\ + (k_i + v_{rv}\sigma_0g_0 - K_0v_{rv}\sigma_0g_0(e^{-\lambda T} - 1))\lambda \\ + k_iv_{rv}\sigma_0g_0 = 0 \end{aligned} \tag{22}$$

where $a_1 = (h_1 + v_{rv}\sigma_0g_0), a_2 = h_1v_{rv}\sigma_0g_0 - v_{rv}g_1h_0h_2 + 1$. Note that Eq. (22) is the transcendental equation because of the appearance of $e^{-\lambda T}$ term. The presence of transcendental terms implies the existence of an infinite number of roots in the complex plane which further determines the stability. If all the roots lie in the left half-plane ($\Re(\lambda) < 0$), then the system is stable. On the other hand, the existence of even one root in the right half-plane ($\Re(\lambda) > 0$) leads to instability in the system.

When the system loses its stability, a pair of complex conjugate roots crosses the imaginary axis ($\Re(\lambda = 0)$), and hence, Hopf bifurcation occurs. Since we are considering the case of Hopf bifurcation in the current analysis, we substitute $\lambda = i\omega$ for $\omega > 0$ in Eq. (22) and separate real and imaginary part to get

$$\begin{aligned} \omega^4 + (-a_2 - K_0 + K_0 \cos(\omega T))\omega^2 \\ - \omega K_0 \sin(\omega T) v_{rv}\sigma_0g_0 + k_iv_{rv}\sigma_0g_0 = 0, \end{aligned} \tag{23a}$$

and

$$\begin{aligned} -a_1\omega^3 - K_0 \sin(\omega T)\omega^2 \\ + (k_i + v_{rv}\sigma_0g_0 - K_0 \cos(\omega T) v_{rv}\sigma_0g_0 \\ + K_0v_{rv}\sigma_0g_0)\omega = 0. \end{aligned} \tag{23b}$$

From Eqs. (23a) and (23b), we can solve for any two control parameters in terms of others and frequency ω . In the current analysis, we solve the above two equations for nondimensional time-delayed feedback gain, K_0 , and time delay T . The control parameters K_0 and T at the Hopf point can be written in terms of other parameters and frequency as

and

$$\begin{aligned} T_{cr} = \frac{1}{\omega} \left(2n\pi + \arctan \left\{ \frac{n_2}{d_2}, \frac{n_1}{d_1} \right\} \right) \\ \forall n = 0, 1, 2, \dots, \infty \end{aligned} \tag{25}$$

where $n_1, n_2, d_1,$ and d_2 are the function of system parameters and defined in ‘Appendix 1,’ n acts as a qualifier for the different stability curves, and subscript ‘ cr ’ signifies values of control parameter at the Hopf point. Also, we ensure that \arctan returns a positive value, so that T_{cr} remains positive. We can note from Eq. (24) that for a finite value of $K_{0,cr}$, the denominator of Eq. (24) should not be equal to zero, i.e.,

$$\omega^6 + (v_{rv}\sigma_0g_0a_1 - a_2)\omega^4 - \omega^2v_{rv}^2\sigma_0^2g_0^2 \neq 0. \tag{26}$$

From the above equation, we solve for ω in terms of other parameters and obtain

$$\omega_1 = \frac{1}{2} \sqrt{2\sqrt{(v_{rv}\sigma_0g_0a_1 - a_2)^2 + 4\omega^2v_{rv}^2\sigma_0^2g_0^2} - 2(v_{rv}\sigma_0g_0a_1 - a_2)}. \tag{27}$$

Therefore, for the finite values of $K_{0,cr}$ and T_{cr} , the permissible range of ω becomes $(\omega_1, \omega_2]$ with $\omega_1 < \omega_2 < \infty$. Further, the stability of steady states in the parametric space of $K_0 - T$ is determined by calculating the real part of the rate of change of eigenvalue, λ , with respect to one of the parameters (K_0, T) at the Hopf point. If the real part of the rate of change of eigenvalue

at the Hopf point is positive, then the steady states lose stability at the Hopf point. If it is negative, then the steady states gain stability at the Hopf point.

Since the solution of the linearized equation of system (given by Eq. 19) will be a periodic solution at the Hopf point, it can be written in terms of eigenvectors as

$$\mathbf{y}(\tau) = A_1 \mathbf{r}_1 e^{i\omega\tau} + A_2 \mathbf{r}_2 e^{-i\omega\tau} \tag{28}$$

where $\mathbf{y}(\tau) = [y_1(\tau), y_2(\tau), y_3(\tau), y_4(\tau)]^T$, A_1 , and A_2 are the arbitrary complex conjugate constants (for the real values of $\mathbf{y}(\tau)$), and \mathbf{r}_1 and \mathbf{r}_2 are the right eigenvectors of characteristic matrix corresponding to eigenvalues $\lambda = i\omega$ and $\lambda = -i\omega$, respectively. The right eigenvector \mathbf{r}_1 for our system is

$$\mathbf{r}_1 = \begin{bmatrix} 1 \\ i\omega \\ -i/\omega \\ Re_1 + iIm_1 \end{bmatrix}, \tag{29}$$

where Re_1 and Im_1 are defined in ‘Appendix 1.’ It should be noted here that the right eigenvector \mathbf{r}_2 (corresponding to eigenvalue $\lambda = -i\omega$) is the complex conjugate of \mathbf{r}_1 and, hence, not reported here for the sake of brevity. For the nonlinear analysis of our coupled system of equations, we also require the generalized left eigenvectors for the removal of secular terms [42]. Therefore, we also determine the left eigenvectors of the characteristic matrix corresponding to eigenvalues $\lambda = i\omega$ and $\lambda = -i\omega$, and these are

$$\mathbf{l}_1 = [1 \quad Lre_1 + iLim_1 \quad Lre_2 + iLim_2 \quad Lre_3 + iLim_3] \tag{30}$$

corresponding to the eigenvalue $\lambda = i\omega$ and its complex conjugate as \mathbf{l}_2 for the eigenvalue $\lambda = -i\omega$. Lre_n and Lim_n , for $n = 1, 2, 3$, are function of system and control parameters, and they are defined in ‘Appendix 1.’ Next we present the nonlinear analysis of our system using the method of multiple scales.

4 Nonlinear analysis using the method of multiple scales

From the linear analysis of our system, we observe that the steady states of the precision motion stage remain stable for small perturbations in the linearly stable regime (perturbations die out with time and settle down to steady states) and becomes unstable (limit cycles/unbounded growth) in the unstable

regime. However, the evolution of the perturbation with time truly depends on the nonlinearities present in the system. If all the perturbations decay with time (irrespective of the amplitude) and settle down to steady states in the linearly stable regime, then the steady states are globally stable. However, if small perturbations decay to steady states and large perturbations lead to limit cycles in the linearly stable regime, then the steady states will no longer be globally stable in the linearly stable regime. Since the above-mentioned dynamical phenomenon depends on the nature of nonlinearity present in the system, it is required to carry out nonlinear analysis of our system, specifically around the stability boundaries, to ascertain the global stability of steady states and, hence, the nature of Hopf bifurcation.

For the nonlinear analysis, we use the method of multiple scales (MMS) for the case of pure slipping motion and obtain the amplitude of limit cycles emerging from the Hopf point. Following the procedure mentioned in [40], we first start with defining multiple timescales as

$$T_0 = \tau, \quad T_1 = \epsilon\tau, \quad T_2 = \epsilon^2\tau, \dots \tag{31}$$

with T_0 as the fast timescale, and T_i (for $i = 1, 2, \dots$) are the slow timescales. With the introduction of these timescales, the derivative operator gets perturbed to the following forms

$$\frac{d}{d\tau} = D_0 + \epsilon D_1 + \epsilon^2 D_2 + \mathcal{O}(\epsilon^3), \tag{32}$$

$$\frac{d^2}{d\tau^2} = D_{0,0} + 2\epsilon D_{0,1} + \epsilon^2 (2D_{0,2} + D_{1,1}) + \mathcal{O}(\epsilon^3), \tag{33}$$

where $D_n = \frac{\partial}{\partial T_n}$ and $D_{m,n} = \frac{\partial^2}{\partial T_m \partial T_n}$. Due to the introduction of multiple timescales in the system, the solution of our perturbed nonlinear equation (Eq. 18) can be assumed to be a series in powers of ϵ till $\mathcal{O}(\epsilon^2)$ and written as

$$\mathbf{y}(\tau) = \mathbf{y}_0(T_0, T_1, T_2) + \epsilon \mathbf{y}_1(T_0, T_1, T_2) + \epsilon^2 \mathbf{y}_2(T_0, T_1, T_2) = \mathbf{y}_0 + \epsilon \mathbf{y}_1 + \epsilon^2 \mathbf{y}_2. \tag{34}$$

Accordingly, the delayed value of the solution $\mathbf{y}(\tau - T)$ can be written as

$$\mathbf{y}(\tau - T) = \mathbf{y}_0(T_0 - T, T_1 - \epsilon T, T_2 - \epsilon^2 T) + \epsilon \mathbf{y}_1(T_0 - T, T_1 - \epsilon T, T_2 - \epsilon^2 T)$$

$$+ \epsilon^2 \mathbf{y}_2 (T_0 - T, T_1 - \epsilon T, T_2 - \epsilon^2 T), \tag{35}$$

$$= \mathbf{y}_{0,T} + \epsilon (-D_1 \mathbf{y}_{0,T} T + \mathbf{y}_{1,T}) + \epsilon^2 \left(\frac{1}{2} D_{1,1} \mathbf{y}_{0,T} T^2 - D_2 \mathbf{y}_{0,T} T - D_1 \mathbf{y}_{1,T} T + \mathbf{y}_{2,T} \right), \tag{36}$$

where $\mathbf{y}(\tau) = [y_1(\tau), y_2(\tau), y_3(\tau), y_4(\tau)]^T$, $\mathbf{y}_m = \mathbf{y}_m(T_0, T_1, T_2) = [y_{1,m}(T_0, T_1, T_2), y_{2,m}(T_0, T_1, T_2), y_{3,m}(T_0, T_1, T_2), y_{4,m}(T_0, T_1, T_2)]^T$ and $\mathbf{y}_{m,T} = \mathbf{y}_m(T_0 - T, T_1, T_2)$ for $m = 0, 1, 2$. The second equality in Eq. (36) is obtained by expanding it in Taylor series for small values of ϵ . Now, to understand the nature of Hopf bifurcation on the stability boundaries we perturb one of the control parameters close to the Hopf point. For the current analysis, we choose time-delay T as the bifurcation parameter and, accordingly, perturb T as

$$T = T_{cr} + \epsilon^2 k_1, \tag{37}$$

where T_{cr} is the value of T at the Hopf point with $K_0 = K_{cr}$. The sign of k_1 is chosen such that T always lies in the unstable regime. Therefore, k_1 can be negative or positive, depending on the location of the unstable region with respect to the Hopf point.

Next, we substitute Eqs. (32)–(37) in Eq. (18), expand in Taylor series for smaller values of ϵ , and equate the coefficients of different orders of ϵ to zero to get coupled constant delay differential equations at different orders of ϵ :

$\mathcal{O}(\epsilon^0)$:

$$D_0 (y_{1,0}) - y_{2,0} = 0, \tag{38a}$$

$$D_0 (y_{2,0}) + y_{1,0} (1 + K_{0,cr}) + h_2 y_{4,0} + k_i y_{3,0} + h_1 y_{2,0} - K_{0,cr} y_{1,0, T_{cr}} = 0, \tag{38b}$$

$$D_0 (y_{3,0}) - y_{1,0} = 0, \tag{38c}$$

$$D_0 (y_{4,0}) + v_{rv} \sigma_0 g_0 y_{4,0} + v_{rv} g_1 h_0 y_{2,0} = 0. \tag{38d}$$

$\mathcal{O}(\epsilon^1)$:

$$D_0 (y_{1,1}) - y_{2,1} = -D_1 (y_{1,0}), \tag{39a}$$

$$D_0 (y_{2,1}) + y_{1,1} (1 + K_{0,cr}) + h_2 y_{4,1} + k_i y_{3,1} + h_1 y_{2,1} - K_{0,cr} y_{1,1, T_{cr}} = h_0 h_3 \sigma_1 y_{2,0}^2 + h_4 \sigma_1 y_{2,0} y_{4,0} - K_{0,cr} T_{cr} D_1 (y_{1,0, T_{cr}}) - D_1 (y_{2,0}), \tag{39b}$$

$$D_0 (y_{3,1}) - y_{1,1} = -D_1 (y_{3,0}), \tag{39c}$$

$$D_0 (y_{4,1}) + v_{rv} \sigma_0 g_0 y_{4,1} + v_{rv} g_1 h_0 y_{2,1} = -h_0 h_3 y_{2,0}^2 + h_4 y_{2,0} y_{4,0} - D_1 (y_{4,0}). \tag{39d}$$

$\mathcal{O}(\epsilon^2)$:

$$D_0 (y_{1,2}) - y_{2,2} = -D_2 (y_{1,0}) - D_1 (y_{1,1}) \tag{40a}$$

$$D_0 (y_{2,2}) + y_{1,2} (1 + K_{0,cr}) + h_2 y_{4,2} + k_i y_{3,2} + h_1 y_{2,2} - K_{0,cr} y_{1,2, T_{cr}} = \sigma_1 h_5 y_{2,0}^3 - D_1 (y_{2,1}) + K_{0,cr} (-D_0 (y_{1,0, T_{cr}}) k_1 - D_2 (y_{1,0, T_{cr}}) T_{cr} + 1/2 D_{1,1} (y_{1,0, T_{cr}}) T_{cr}^2) + \sigma_1 h_4 y_{2,1} y_{4,0} + \sigma_1 h_4 y_{2,0} y_{4,1} + 2 h_0 \sigma_1 h_3 y_{2,0} y_{2,1} - D_2 (y_{2,0}) + \sigma_1 \sigma_0 h_3 y_{2,1}^2 y_{4,1} - K_{0,cr} D_1 (y_{1,1, T_{cr}}) T_{cr}, \tag{40b}$$

$$D_0 (y_{3,2}) - y_{1,2} = -D_2 (y_{3,0}) - D_2 (y_{3,1}) \tag{40c}$$

$$D_0 (y_{4,2}) + v_{rv} \sigma_0 g_0 y_{4,2} + v_{rv} g_1 h_0 y_{2,2} = -h_4 y_{2,1} y_{4,0} - h_5 y_{2,0}^3 - D_2 (y_{4,0}) - D_1 (y_{4,1}) - 2 h_0 h_3 y_{2,0} y_{2,1} - \sigma_0 h_3 y_{2,0}^2 y_{4,0} + h_4 y_{2,0} x_{4,1}. \tag{40d}$$

We note that the equations at the order of ϵ^0 (Eq. 38) are identical to linearized unperturbed equations (Eq. 19) with the control parameters at the Hopf point. Therefore, the solution for the equations at the order of ϵ^0 (Eq. 38) can be formulated as

$$\mathbf{y}_0 (T_0, T_1, T_2) = A_1 (T_1 T_2) \mathbf{r}_1 e^{i\omega T_0} + A_2 (T_1 T_2) \mathbf{r}_2 e^{-i\omega T_0}, \tag{41}$$

where A_1 and A_2 instead of being complex conjugate constants are now complex conjugate function of slow timescales T_1 and T_2 . On the substitution of the assumed form of the solution for \mathbf{y}_0 in the equations corresponding to ϵ^1 (Eq. 39), we observe the appearance of $e^{2i\omega T_0}$, $e^{-2i\omega T_0}$, $e^{i\omega T_0}$ and $e^{-i\omega T_0}$ on the right side of the equations. Note that terms $e^{i\omega T_0}$ and $e^{-i\omega T_0}$ act as resonant forcing terms, further causing an unbounded growth in the solution for \mathbf{y}_1 and known as secular terms. Therefore, to get the bounded solution for the \mathbf{y}_1 , the removal of these secular terms from the equations is necessary. Removal of these secular terms requires that the dot product of left eigenvectors corresponding

to $e^{i\omega T_0}$ and $e^{-i\omega T_0}$ with the vectors consisting coefficient of $e^{i\omega T_0}$ and $e^{-i\omega T_0}$ set to be zero [42]. The coefficient vectors \mathbf{u}_1 and \mathbf{u}_2 corresponding to $e^{i\omega T_0}$ and $e^{-i\omega T_0}$ are

$$\mathbf{u}_1 = \frac{\partial A_1(T_1, T_2)}{\partial T_1} \begin{bmatrix} 1 \\ u_{11} + iu_{12} \\ -i \\ \omega \\ u_{21} + iu_{22} \end{bmatrix}, \text{ and}$$

$$\mathbf{u}_2 = \frac{\partial A_1(T_1, T_2)}{\partial T_1} \begin{bmatrix} 1 \\ u_{11} - iu_{12} \\ i \\ \omega \\ u_{21} - iu_{22} \end{bmatrix}, \tag{42}$$

where u_{11} , u_{12} , u_{21} , and u_{22} are defined in ‘Appendix 2.’ It should be noted here that \mathbf{u}_1 and \mathbf{u}_2 are complex conjugate of each other, respectively. Removal of secular terms corresponding to $e^{i\omega T_0}$ at $\mathcal{O}(\epsilon)$ leads to

$$\mathbf{l}_1 \cdot \mathbf{u}_1 = 0 \tag{43}$$

which further leads to

$$\begin{aligned} &\frac{\partial A_1(T_1, T_2)}{\partial T_1} \left(1 + Lre_1 u_{11} - Lim_1 u_{12} + \frac{Lim_2}{\omega} \right. \\ &\quad \left. + Lre_3 u_{21} - Lim_3 u_{22} \right. \\ &\quad \left. + i \left(Lre_1 u_{12} + Lim_1 u_{11} - \frac{Lre_2}{\omega} \right. \right. \\ &\quad \left. \left. + Lre_3 u_{22} + Lim_3 u_{21} \right) \right) = 0. \end{aligned} \tag{44}$$

Since the term inside the brackets is not zero for a general value of system and control parameters, we get

$$\frac{\partial A_1(T_1, T_2)}{\partial T_1} = 0. \tag{45}$$

Similarly, the second equation corresponding to removal of secular terms for $e^{-i\omega T_0}$ at $\mathcal{O}(\epsilon)$, i.e., $\mathbf{l}_2 \cdot \mathbf{u}_2 = 0$, leads to $\frac{\partial A_2(T_1, T_2)}{\partial T_1} = 0$. The above solutions for $A_1(T_1, T_2)$ and $A_2(T_1, T_2)$ do not provide any additional information except that A_1 and A_2 do not depend on the slow timescale T_1 . These results also suggest that to get a nontrivial solutions for A_1 and A_2 , we need to proceed to the equations corresponding to the order of ϵ^2 . However, before proceeding to the next order, we need solution for \mathbf{y}_1 at $\mathcal{O}(\epsilon^1)$.

To get the solution at $\mathcal{O}(\epsilon^1)$ for \mathbf{y}_1 , we use the method of harmonic balance. After substituting the solution for \mathbf{y}_0 in Eq. (39) with the fact that the solutions for A_1 and A_2 are independent of T_1 , we substitute the following assumed form of the solution for \mathbf{y}_1

$$\begin{aligned} \mathbf{y}_1(T_0, T_1, T_2) &= A_1^2(T_2) \mathbf{B}_{11} e^{2i\omega T_0} \\ &\quad + A_2^2(T_2) \mathbf{B}_{22} e^{-2i\omega T_0} \\ &\quad + A_1(T_2) A_2(T_2) \mathbf{B}_{12}, \end{aligned} \tag{46}$$

where coefficient vectors \mathbf{B}_{11} , \mathbf{B}_{22} , and \mathbf{B}_{12} are defined as

$$\mathbf{B}_{11} = \begin{bmatrix} b_{11} \\ b_{12} \\ b_{13} \\ b_{14} \end{bmatrix}, \quad \mathbf{B}_{22} = \begin{bmatrix} b_{21} \\ b_{22} \\ b_{23} \\ b_{24} \end{bmatrix}, \text{ and}$$

$$\mathbf{B}_{12} = \begin{bmatrix} b_{31} \\ b_{32} \\ b_{33} \\ b_{34} \end{bmatrix}. \tag{47}$$

On substituting the assumed form of the solution for \mathbf{y}_1 and doing harmonic balance, we get 12 algebraic simultaneous equations in terms of b_{mn} (for $m = 1, 2, 3$ and $n = 1, 2, 3, 4$). On solving these equations we observe that elements of vectors \mathbf{B}_{11} and \mathbf{B}_{22} are complex conjugate of each other. Therefore, for sake of brevity we only report coefficients of \mathbf{B}_{11} and \mathbf{B}_{12} in ‘Appendix 2.’ Next, we substitute the solutions for \mathbf{y}_0 and \mathbf{y}_1 in terms of $A_1(T_2)$ and $A_2(T_2)$ in the equations corresponding to $\mathcal{O}(\epsilon^2)$. Again, the secular terms in the resulting equations can be removed using the solvability conditions of $\mathbf{l}_1 \cdot \mathbf{V}_1 = 0$ and $\mathbf{l}_2 \cdot \mathbf{V}_2 = 0$, where \mathbf{V}_1 and \mathbf{V}_2 are the complex conjugate vectors with the coefficients corresponding to $e^{i\omega T_0}$ and $e^{-i\omega T_0}$, respectively. These vectors are

$$\mathbf{V}_1 = \begin{bmatrix} \frac{\partial A_1(T_2)}{\partial T_2} \\ \frac{\partial A_1(T_2)}{\partial T_2} v_{11} + v_{12} \\ -\frac{i}{\omega} \frac{\partial A_1(T_2)}{\partial T_2} \\ \frac{\partial A_1(T_2)}{\partial T_2} v_{21} + v_{22} \end{bmatrix} \text{ and}$$

$$\mathbf{V}_2 = \begin{bmatrix} \frac{\partial A_2(T_2)}{\partial T_2} \\ \frac{\partial A_2(T_2)}{\partial T_2} \bar{v}_{11} + \bar{v}_{12} \\ \frac{i}{\omega} \frac{\partial A_2(T_2)}{\partial T_2} \\ \frac{\partial A_2(T_2)}{\partial T_2} \bar{v}_{21} + \bar{v}_{22} \end{bmatrix}, \tag{48}$$

where v_{mn} are defined in ‘Appendix 2.’ Since \bar{v}_{mn} are complex conjugate of v_{mn} , they are not reported in the paper for sake of brevity. Next, we switch to polar coordinates by substituting

$$A_1(T_2) = \frac{R(T_2)e^{i\phi(T_2)}}{2} \quad \text{and}$$

$$A_2(T_2) = \frac{R(T_2)e^{-i\phi(T_2)}}{2}, \quad (49)$$

into the equation resulting from $\mathbf{l}_1 \cdot \mathbf{V}_1 = 0$ and separate real and imaginary parts. On separating real and imaginary parts we get two equations and can be solved for $\partial R(T_2)/\partial T_2$ and $\partial \phi(T_2)/\partial T_2$ as

$$\frac{\partial R(T_2)}{\partial T_2} = p_{11}k_1R + p_{12}R^3, \quad (50)$$

$$\frac{\partial \phi(T_2)}{\partial T_2} = p_{21}k_1 + p_{22}R^2, \quad (51)$$

where p_{11} , p_{12} , p_{21} , and p_{22} are functions of system parameters, control parameters at the Hopf point, and frequency (ζ , σ_0 , σ_1 , σ_2 , f_s , f_c , a , T_{cr} , $K_{0,cr}$, ω). Since the functional forms of these terms are very lengthy, these are not reported in the paper for sake of brevity. Finally, the equation governing the evolution of amplitude R and phase ϕ in the original timescale τ can be written using Eq. (32) as

$$\frac{dR}{d\tau} = \epsilon \frac{\partial R}{\partial T_1} + \epsilon^2 \frac{\partial R}{\partial T_2} = \epsilon \left(p_{11}k_1R + p_{12}R^3 \right)$$

$$\frac{\partial \phi}{\partial T_2} = \epsilon^2 \frac{\partial \phi}{\partial T_1} + \epsilon^2 \frac{\partial \phi}{\partial T_2} = \epsilon^2 \left(p_{21}k_1 + p_{22}R^2 \right). \quad (52)$$

Accordingly, the solution in the original variables $x_i(\tau)$ can be obtained by utilizing Eqs. (17), (34), (41), (49), and (52). Note that Eq. (52) can also be used to determine the amplitude and stability of limit cycles originating from Hopf point which further dictates the nature of Hopf bifurcation. A detailed discussion on these slow flow equations and verification of our analytical approach with numerical simulation is presented in the next section.

5 Results and discussion

In this section, we first present results on the linear stability of the steady states of MBMS, which also provides information about the Hopf point for the results of nonlinear analysis. Later on, we present the analytical results using the method of multiple scales, which are verified with numerical simulations.

Table 1 Scales and nondimensional parameters used in the simulation

ω_0 (rad/s)	115.5	X_0 (m)	0.00073
σ_0	110	σ_1	1.37
σ_2	0.0823	f_s	0.44
f_c	0.35	a	2.5

5.1 Linear stability curves

For the linear and nonlinear analysis, we have used the parameter values given in Table 1 ([34]). Since ζ , k_i , T , K_0 , and v_{rv} vary, the numerical values of these are not reported in Table 1. The linear stability curves produced on the control parameter space of $T - K_0$ are shown in Figs. 3, 4, 5, and 6. These curves are produced using Eqs. (24)–(25) by varying frequency, ω , in a range of $\omega \in (\omega_1, \omega_2]$ (where ω_1 is defined in Eq. (27) and $\omega_1 < \omega_2 < \infty$). Since the effect of v_{rv} on the stability of such systems has been already analyzed in [40], we focus on analyzing the effect of differential gain (ζ) and integral gain (k_i) on the stability of steady states for a fixed value of v_{rv} . Thus, multiple stability curves are produced for different combinations of ζ and k_i to get a complete understanding of the dynamics of the system. In these stability curves, the stable regions are marked by ‘S,’ while the unstable regions are marked by ‘U.’

As mentioned earlier, the stability boundaries in the control parameter space of $T - K_0$ are obtained using Eqs. (24)–(25) by varying $\omega \in (\omega_1, \omega_2]$. For this range of ω , multiple stability lobes exist corresponding to different values of $n = 0, 1, 2, \dots, \infty$ (see Eq. 25). Furthermore, there is a huge possibility of interactions between the multiple stability lobes corresponding to different values of n for the given values of ζ , k_i , and v_{rv} . Due to the interaction of multiple lobes with each other, the primary/overall stability boundary is obtained by taking the union of various stability lobes ($n = 0, 1, 2, \dots$). In this scenario, the effective range of ω , for each stability lobe, is different and leads to the existence of codimension-2 Hopf points. For example, in Fig. 3i for $\zeta = 0.05$ and $k_i = 0.001$, the first stability lobe on the primary stable regime is obtained by varying ω in a range of [5.243, 0.9975780], while the second stability lobe is obtained by varying ω in [3.492, 0.9977897]. At the interaction of these two stability lobes, two frequencies, viz. $\omega = 0.9975780$ and

Fig. 3 Stability curves in $(T - K_0)$ space for $\sigma_0 = 110, \sigma_1 = 1.37, \sigma_2 = 0.0823, f_s = 0.44, f_c = 0.35, v_{rv} = 0.1, \zeta = 0.05,$ and $a = 2.5$ with different values of k_i corresponding to (i) multiple lobes, (ii) single lobe

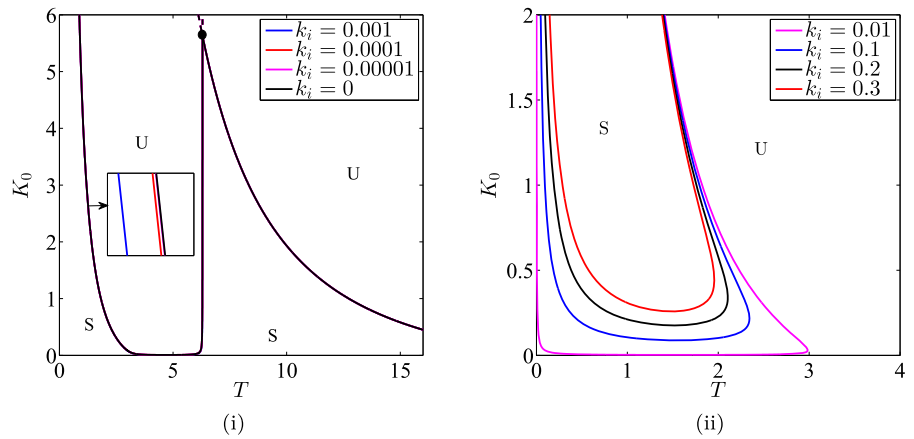


Fig. 4 Stability curves in $(T - K_0)$ space for $\sigma_0 = 110, \sigma_1 = 1.37, \sigma_2 = 0.0823, f_s = 0.44, f_c = 0.35, v_{rv} = 0.1, \zeta = 0.1,$ and $a = 2.5$ with different values of k_i corresponding to (i) multiple lobes, (ii) single lobe

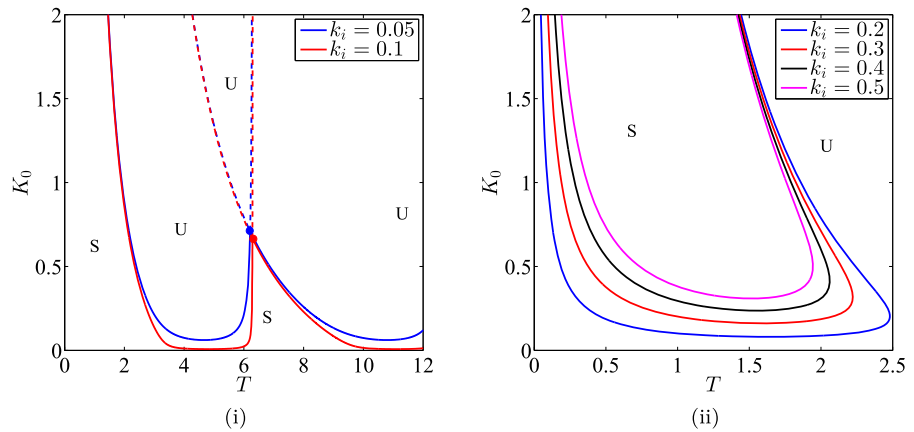
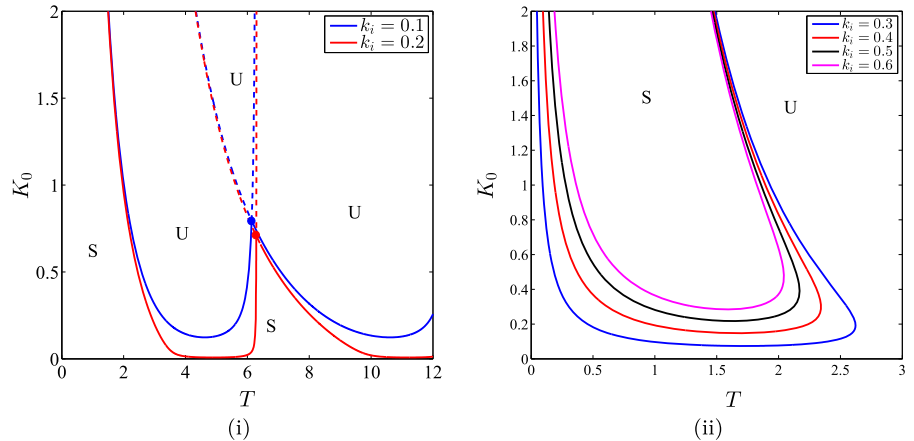


Fig. 5 Stability curves in $(T - K_0)$ space for $\sigma_0 = 110, \sigma_1 = 1.37, \sigma_2 = 0.0823, f_s = 0.44, f_c = 0.35, v_{rv} = 0.1, \zeta = 0.15,$ and $a = 2.5$ with different values of k_i corresponding to (i) multiple lobes, (ii) single lobe

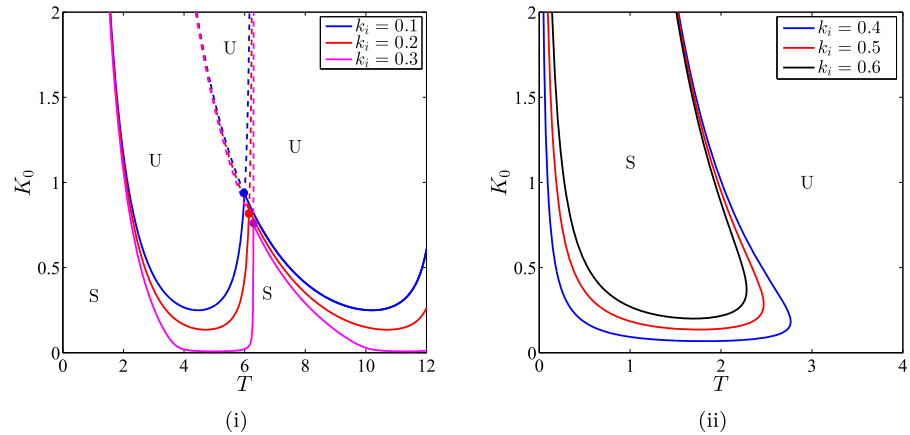


$\omega = 3.492,$ coexist, leading to the codimension-2 Hopf point (marked with filled circles in stability curves). Therefore, the information about the effective range of ω for each stability lobe is important to extract the overall stability boundary in parametric space. In a similar trend, other stability boundaries corresponding to dif-

ferent values of n interact and, hence, result in multiple codimension-2 Hopf points.

The variation of stability curves with k_i for different values of ζ is shown in Figs. 3, 4, 5, and 6. From these stability curves, we can easily observe that for each value of $\zeta,$ there exists a critical value of $k_i,$ say $\bar{k}_i,$

Fig. 6 Stability curves in $(T - K_0)$ space for $\sigma_0 = 110$, $\sigma_1 = 1.37$, $\sigma_2 = 0.0823$, $f_s = 0.44$, $f_c = 0.35$, $v_{rv} = 0.1$, $\zeta = 0.2$, and $a = 2.5$ with different values of k_i corresponding to (i) multiple lobes, (ii) single lobe



below which multiple stability lobes (corresponding to different values of n) interact and the overall stability boundary is the combination of multiple stability lobes (see Figs. 3a, 4a, 5a, 6a). In Figs. 3i–6i, part of stability lobes that contributes to the overall stability region is shown by a solid line otherwise by a dashed line, and different codimension-2 Hopf points are shown using filled circles. However, we also emphasize here that for the values of $k_i < \bar{k}_i$, stability lobe corresponding to $n = 0$ does not contribute in the stable region as it lies on the negative half-plane of T , and for practical application of time-delayed feedback control negative values of T are not feasible. Furthermore, as the value of k_i reaches the value of \bar{k}_i , the interaction between the stability lobes decreases, leading to the vanishing of codimension-2 Hopf point. We observe that for a given value of ζ as k_i approaches the value of \bar{k}_i , the stability regime decreases as the minimum value of $K_{0,cr}$ (Hopf point on the stability lobe) decreases. Therefore, without any loss of generality we can assume that at $k_i = \bar{k}_i$, $\min(K_{0,cr})$ will be zero. With this assumption, we get an implicit equation in terms of k_i , ζ , and ω from Eq. (24) and can be solved for real values of \bar{k}_i and ω with a given value of ζ or vice versa.

From Figs. 3ii, 4ii, 5ii, and 6ii we observe that as k_i crosses the value of \bar{k}_i , there are no interactions between the stability lobes, and therefore, there are no codimension-2 Hopf points in the system. Also, the primary stability boundaries for these values of k_i are obtained by varying $\omega \in (\omega_1, \omega_2]$ for the stability lobe corresponding to $n = 0$ as the stability lobes for higher values of n are on the extreme right side of stability lobe for $n = 0$ and, hence, do not contribute in the overall stability of the system. However, as the value

of k_i further increases, the overall stability decreases as evident from Figs. 3ii, 4ii, 5ii, and 6ii.

Before proceeding further to ascertain the nature of bifurcation on the stability lobes and amplitude of limit cycles from the slow flow equations close to Hopf point, it is required to validate analytical results with numerical simulation. For numerical simulation, MATLAB routine ‘dde23’ can be used; however, the use of ‘dde23’ is restricted in the fixed-arc-length-based continuation scheme to get the unstable branch of solutions. Therefore, we adopt the approach developed by Wahi and Chatterjee [43] and convert the infinite-dimensional time-delayed system to the finite-dimensional system of ordinary differential equations (odes) using Galerkin projection. This is presented in the next section.

5.2 Galerkin projection of delay differential equation (DDE)

We note that to solve our set of DDE at time $\tau = 0$, we need to define an initial function, let us say $g(s)$, over the period $\tau \in [-T, 0]$ such that $g(s) = x(-s)$ for $s \in [0, T]$. Now, as the system evolves with time τ , we need to keep track of the delayed value of the response in the immediate previous interval $\tau \in [\tau - T, \tau]$ to capture the response at time instant τ . To ease this process Wahi and Chatterjee [43] proposed another method by parameterizing the delay with an introduction of variable ‘s’ and function F such that

$$x(\tau - s) = F(\tau, s) \quad s \in [0, T]. \quad (53)$$

Now, with the introduction of variable ‘s’ and function ‘F’ we can easily observe that

$$x(\tau) = F(\tau, 0) \quad \text{and} \quad x(\tau - T) = F(\tau, T). \quad (54)$$

It is a well-known fact that any smooth function can be expressed in terms of a Fourier sine series superimposed on a straight line. Using this, we approximate $F(\tau, s)$ by

$$F(\tau, s) = a_0(\tau) + a_1(\tau) \frac{s}{T} + \sum_{k=1}^{N-1} a_{k+1} \sin\left(\frac{k\pi s}{T}\right), \quad (55)$$

where N represents the number of terms in the approximation and $a_p(\tau)$ represents the undetermined function of time τ that define $F(\tau, s)$, and eventually $x(\tau)$ and $x(\tau - T)$ in the following manner

$$x(\tau) = F(\tau, 0) = a_0(\tau), \quad (56)$$

$$x(\tau - T) = F(\tau, T) = a_0(\tau) + a_1(\tau). \quad (57)$$

The evolution of function F over the period of time can be obtained utilizing Eq. (53)

$$\frac{\partial F}{\partial \tau} + \frac{\partial F}{\partial s} = 0. \quad (58)$$

On substituting F from Eq. (55) in the above evolution equation for F , we get

$$\begin{aligned} \dot{a}_0(\tau) + \dot{a}_1(\tau) \frac{s}{T} + \sum_{k=1}^{N-1} \dot{a}_{k+1}(\tau) \sin\left(\frac{k\pi s}{T}\right) \\ + \left\{ a_1(\tau) \frac{1}{T} + \sum_{k=1}^{N-1} \frac{a_{k+1}(\tau) k\pi}{T} \cos\left(\frac{k\pi s}{T}\right) \right\} \\ = 0, \end{aligned} \quad (59)$$

where overhead dot represents the derivative with respect to time τ . It is to be noted here that the above equation is not satisfied identically and, hence, the left side of Eq. (59) represents the residue, R_e , as

$$\begin{aligned} R_e = \dot{a}_0(\tau) + \dot{a}_1(\tau) \frac{s}{T} + \sum_{k=1}^{N-1} \dot{a}_{k+1}(\tau) \sin\left(\frac{k\pi s}{T}\right) \\ + \left\{ a_1(\tau) \frac{1}{T} + \sum_{k=1}^{N-1} \frac{a_{k+1}(\tau) k\pi}{T} \cos\left(\frac{k\pi s}{T}\right) \right\}. \end{aligned} \quad (60)$$

The residue, R_e , can be minimized using the Galerkin projection approach by making it orthogonal to shape

functions corresponding to $a_p(\tau)$ (for $p = 1, 2 \dots N$). This step results in N first-order odes as

$$\int_0^T R_e s ds = 0, \quad (61)$$

$$\int_0^T R_e \sin\left(\frac{k\pi s}{T}\right) ds = 0, \quad (62)$$

for $k = 1, \dots, N - 1$.

These first-order odes, governing the evolution of $a_p(\tau)$ (for $p = 1, 2, \dots N$), along with Eq. (12) (with modified definition of $x(\tau)$ and $x(\tau - T)$) govern the evolution of our system with time τ . Since for the rest of the analysis we will use this approach for numerical simulations, it is necessary to validate it with the solution of original equations (Eq. 12) using MATLAB routine ‘dde23.’ For this purpose, we choose two different sets of parameters in the unstable regime and compare the steady response using phase portrait with $N = 35$ terms in Galerkin approximation (for more details about the convergence of Galerkin approximation readers are referred to [44]). This comparison is shown in Fig. 7, and we can observe that there is an excellent match between the results from ‘dde23’ and Galerkin projection. With this agreement, next we present the validation of our analytical results from MMS with numerical simulation.

5.3 Validation of analytical results from MMS

In this section, we present the validity of the solution from slow flow equations (Eq. 52) by comparing it with numerical simulations. For this, we compare the time response of the system using Galerkin projection with those obtained from the slow flow equation and establish the accuracy of the MMS. To achieve this, we choose two different sets of parameters close to Hopf point such that one point corresponds to the unstable regime ($K_{0,cr} = 0.5, T = 2.8716 > T_{cr} = 2.8715$), while the other point lies in the stable regime ($K_{0,cr} = 0.5, T = 2.8714 < T_{cr} = 2.8715$). Accordingly, we get a gradually increasing periodic response (till it settles down to stable limit cycle) and gradually decreasing periodic response (till it settles down to steady state). From Fig. 8, it can be easily observed that the time response of the system obtained from MMS matches excellently with that obtained numerically. This observation validates our analytical approach.

Fig. 7 Comparison of steady responses using phase portrait of the system obtained from the MATLAB routine ‘dde23’ and Galerkin projection with (i) $K_0 = 0.5, T = 2.9$ (ii) $K_0 = 0.5, T = 6$, with $N = 35$ terms in the Galerkin approximation. The other parameters are $\sigma_0 = 110, \sigma_1 = 1.37, \sigma_2 = 0.0823, f_s = 0.44, f_c = 0.35, v_{rv} = 0.1, \zeta = 0.2, k_i = 0.1$, and $a = 2.5$

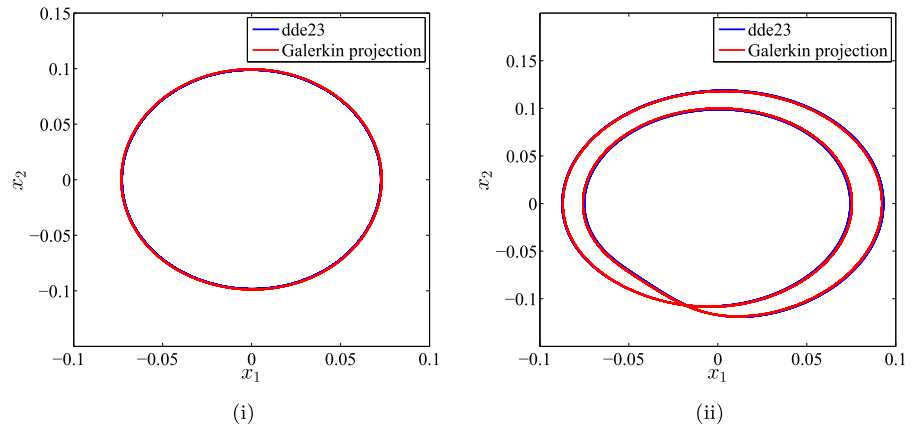
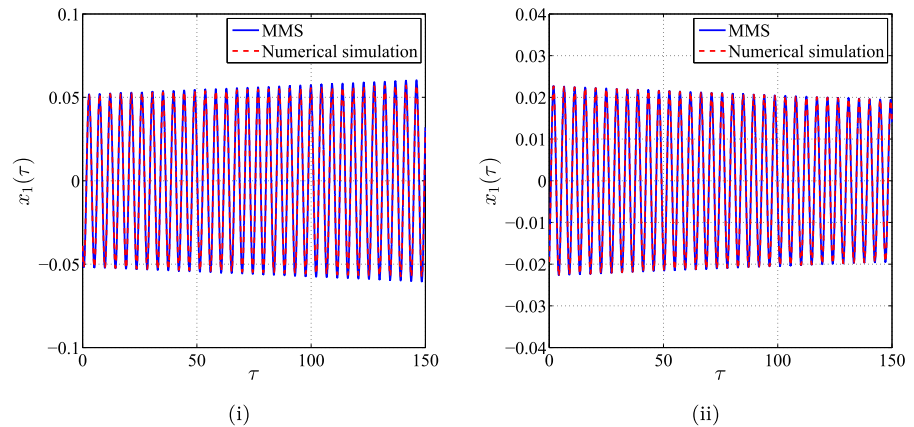


Fig. 8 Comparison of time response of the system obtained from the method of multiple scales (solid line) and numerical simulation (dashed line) with (a) $T = 2.8716 > T_{cr} = 2.8715$, (b) $T = 2.8714 < T_{cr} = 2.8715$. The other parameters are $\sigma_0 = 110, \sigma_1 = 1.37, \sigma_2 = 0.0823, f_s = 0.44, f_c = 0.35, v_{rv} = 0.1, \zeta = 0.2, K_0 = 0.5, k_i = 0.1$, and $a = 2.5$



Having established this agreement, next we present the criticality of Hopf bifurcation on the stability curves.

5.4 Criticality of Hopf bifurcation

In this section, we present the stability lobes with the associated Hopf bifurcation as obtained analytically using MMS. As already discussed, if either of the control parameters K_0 or T changes such that they cross the stability boundaries (T_{cr} and $K_{0,cr}$) and move from stable to unstable, the system loses its stability through Hopf bifurcation and settles down to stable vibratory response (or stable limit cycles). The amplitude of these stable limit cycles can be determined with the help of slow flow equations (Eq. 52) and, eventually, the nature of bifurcation. If stable limit cycles, close to Hopf point, exist in the unstable regime, then the bifurcation is supercritical in nature, which further implies that the system is globally stable and the nonlinearity in the system is stabilizing in nature. However, the exist-

tence of small-amplitude unstable limit cycles in the linearly stable regime leads to subcritical bifurcation and, eventually, loss of global stability. Therefore, in the linear stable regime small perturbation decays, while sufficiently large perturbation grows to large-amplitude solution for a subcritical bifurcation and leading to loss of global stability.

To determine the global stability of steady states close to Hopf point and, eventually, the nature of Hopf bifurcation, we need to determine the steady-state amplitude of limit cycles. The amplitude of limit cycles close to Hopf point can be obtained by nontrivial fixed points of the slow flow equations, i.e., by setting $\dot{R} = 0$ in Eq. (52). Therefore, the nontrivial fixed point of Eq. (52) or the amplitude of limit cycles close to Hopf point is given by

$$R = \sqrt{\frac{-p_{11}k_1}{p_{12}}}. \tag{63}$$

It should be noted here that quantity $p_{11}k_1$ always remains positive in the linear unstable regime and neg-

ative in the linear stable regime. Therefore, the nature of Hopf bifurcation is governed by the sign of p_{12} only. If p_{12} is negative, then limit cycles will exist in linearly unstable regimes only and the Hopf bifurcation will be supercritical in nature. However, if p_{12} becomes positive, then the limit cycles will exist in the linear stable regimes, and the Hopf bifurcation will be subcritical in nature. Therefore, the set of control parameters on the stability boundary corresponding to transition point from subcritical to supercritical or vice versa can be found by setting denominator to 0, i.e.,

$$p_{12}(\zeta, \sigma_0, \sigma_1, \sigma_2, f_s, f_c, a, T_{cr}, K_{0,cr}, \omega) = 0. \tag{64}$$

We substitute T_{cr} and $K_{0,cr}$ from Eqs. (24) and (25) in Eq. (64) and get a transcendental equation in terms of system parameters and frequency. The resulting transcendental equation can be solved for critical frequency, ω_{cr} , corresponding to the transition point. However, as the analytical form of p_{12} is very lengthy, it is very difficult to obtain the closed-form solution for ω_{cr} , and hence, we resort to numerical technique after substitution of numerical values of the system parameters and n . Accordingly, the numerical values of control parameters K_0 and T corresponding to the transition point can be obtained utilizing Eqs. (24) and (25). For $k_i < \bar{k}_i$ we get one positive root of the transcendental equation, in the range of $(\omega_1, \omega_2]$, in the primary stability boundary, for every value of n ($n = 1, 2, \dots$). There is a possibility of multiple roots on the stability lobes; however, as these roots are beyond the codimension-2 Hopf point, i.e., they lie in the unstable region already, they do not play any role in changing the bifurcation. Further, we observe that for $k_i > \bar{k}_i$, there is only one real root of the transcendental equation for $n = 0$, i.e., for the primary stability boundary, and hence, there is only one transition point from subcritical to supercritical or vice versa.

Next, we present the stability boundaries for two different values of k_i , viz. $k_i = 0.1 < \bar{k}_i \approx 0.31$ and $k_i = 0.4 > \bar{k}_i \approx 0.31$ with $\zeta = 0.2$, depicting different regions of supercritical and subcritical bifurcation with blue and red colors, respectively. From Fig. 9, we observe that for $k_i = 0.1$ ($k_i < \bar{k}_i$) there is a continuous transition from supercritical to subcritical bifurcation due to the existence of multiple stability lobes and eventually multiple transition points on the primary stability curve. However, for $k_i = 0.4$ ($k_i > \bar{k}_i$) there is only one transition point existing on the primary stability,

and hence, the primary stability curve is divided into two branches of supercritical and subcritical bifurcation. It is to be noted here that the analytical results using MMS only give information about the amplitude of limit cycles close to Hopf point and do not provide the overall nonlinear global behavior of our system. Therefore, we use numerical bifurcation analysis to get an understanding of the large-amplitude response of the precision motion stage, and this is presented in the next section. This step further acts as another verification of our analytical results.

5.5 Bifurcation analysis

For the numerical bifurcation analysis, we have used built-in MATLAB routine ‘ode45’ with high value of relative and absolute tolerance ‘1e-8’ to solve our $N + 4$ first-order system of odes. The bifurcation diagrams, showing the extrema for x_1 (corresponding to $x_2 = 0$) for two different values of k_i (one corresponding to multiple stability lobes, i.e., $k_i < \bar{k}_i$ and another corresponding to one stability lobe, i.e., $k_i > \bar{k}_i$), are shown in Fig. 10. Note that these bifurcation diagrams can be plotted by fixing either of the control parameters, i.e., K_0 or T and varying other. Since in our analytical analysis we have chosen T as bifurcation parameter, we fix the value of K_0 and vary T in forward and backward direction. However, as the nature of Hopf bifurcation is not observable in Fig. 10, the zoomed views of different sections of these bifurcation diagrams for $k_i = 0.1$ ($< \bar{k}_i \approx 0.31$) and $k_i = 0.4$ ($> \bar{k}_i \approx 0.31$) with $\zeta = 0.2$ are shown in Figs. 11 and 12, respectively.

From the zoomed view of different sections of bifurcation diagrams, we can observe that for $k_i = 0.1$ there are continuous transitions in the nature of Hopf bifurcation because of the existence of multiple stability lobes and eventually, multiple transition points. However, for $k_i = 0.4$, we get only one transition from subcritical to supercritical Hopf bifurcation or vice versa. We note that both of the above-drawn observations for $k_i = 0.1$ and $k_i = 0.4$ are consistent with our analytical observations using MMS. Also, the overall picture of these bifurcation diagrams is very complex due to the existence of alternate regions of steady and vibratory response along with quasi-periodic and period-2 solutions and will be discussed later in this section. It is to be noted here that the current choice of K_0 is sufficiently far away from the codimension-2 Hopf

Fig. 9 Stability boundary in the $T - K_0$ space depicting the supercritical and subcritical branches via blue and red lines, respectively, for (a) $k_i = 0.1$, (b) $k_i = 0.4$. The other parameters for numerical simulations are $\sigma_0 = 110$, $\sigma_1 = 1.37$, $\sigma_2 = 0.0823$, $f_s = 0.44$, $f_c = 0.35$, $v_{rv} = 0.1$, $\zeta = 0.2$, and $a = 2.5$. (Color figure online)

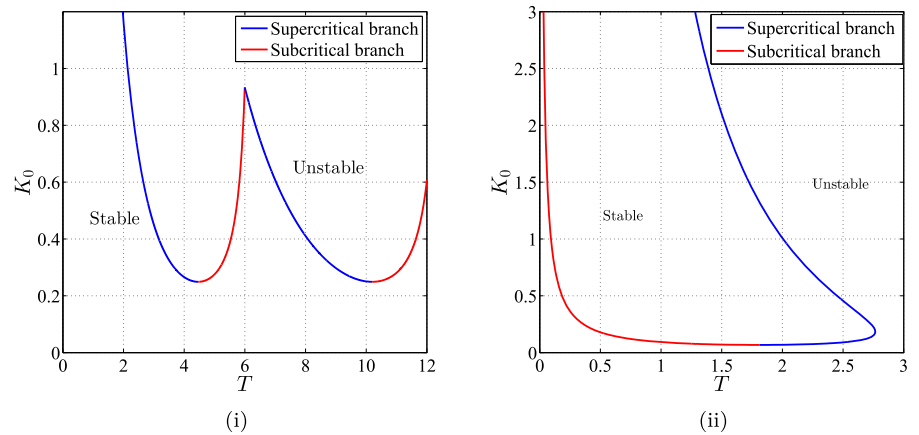
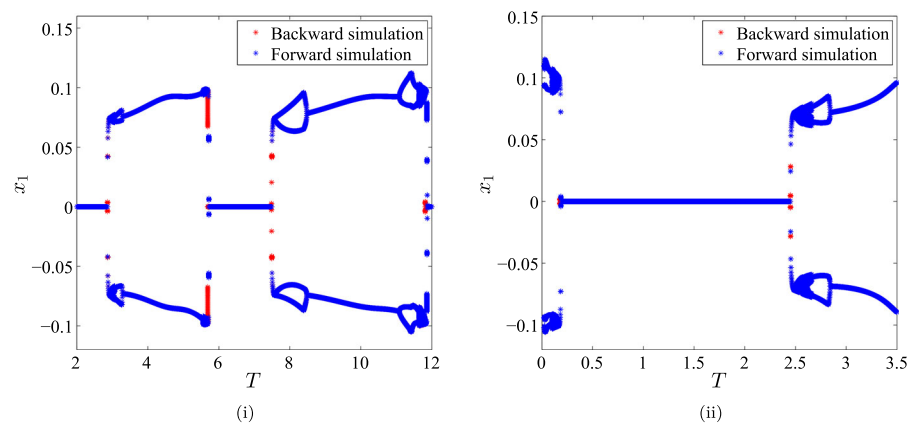


Fig. 10 Numerical bifurcation diagram with T as bifurcation parameter for (i) $k_i = 0.1$, (ii) $k_i = 0.4$. The other parameters are $\sigma_0 = 110$, $\sigma_1 = 1.37$, $\sigma_2 = 0.0823$, $f_s = 0.44$, $f_c = 0.35$, $v_{rv} = 0.1$, $\zeta = 0.2$, $K_0 = 0.5$, and $a = 2.5$



points, and hence, we do not observe complicated high-amplitude chaotic solutions.

After establishing a qualitative match from the analytical and numerical findings, we perform the quantitative match as well. For this step, we have chosen two different values of k_i , viz. $k_i = 0.1 < \bar{k}_i \approx 0.3$ $k_i = 0.4 > \bar{k}_i \approx 0.3$ with $\zeta = 0.2$. We obtained the branch of limit cycles using fixed-arc-length continuation scheme [45]. These results are shown in Figs. 13 and 14 for $k_1 = 0.1$ and $k_i = 0.4$, respectively. In these figures, solid lines represent the stable steady-state response, whereas dashed lines represent unstable steady states. From both figures, we observe that there is a decent match between the numerical results from the continuation method and the MMS results for moderate amplitudes. The coexistence of unstable limit cycles with a stable equilibrium in Figs. 13ii, iv, and 14i indicates that Hopf bifurcation is subcritical in nature. However, from Figs. 13i, iii, and 14ii we

can observe that a stable limit cycle with pure slipping motion exists with unstable equilibrium and signifies supercritical Hopf bifurcation. It can be noted from Figs. 13 and 14 that the subcritical branch of limit cycles undergoes a smooth turning bifurcation resulting in stable limit cycles with large-amplitude stick-slip motion. The illustrative phase portraits for stable limit cycles with stick-slip close to Hopf point are shown in Fig. 15.

Further examination of numerical bifurcation for $k_i = 0.1$ and $k_i = 0.4$ with varying values of T (Figs. 10, 11, 12) reveals the existence of period-2 solutions, quasi-periodic solutions, and eventually, supercritical period-doubling bifurcation near the Hopf point. For an illustration, consider the stable periodic solution for $k_i = 0.1$ and $\zeta = 0.2$ with $K_0 = 0.5$ and $T = 3.3457$ near the first stability lobe. As we decrease the value of T , stable stick-slip limit cycles lose stability through supercritical period-2 bifurcation

Fig. 11 Zoomed view of Fig. 10i with different ranges of T . The other parameters are $\sigma_0 = 110$, $\sigma_1 = 1.37$, $\sigma_2 = 0.0823$, $f_s = 0.44$, $f_c = 0.35$, $v_{rv} = 0.1$ $\zeta = 0.2$, $K_0 = 0.5$, $k_i = 0.1$, and $a = 2.5$

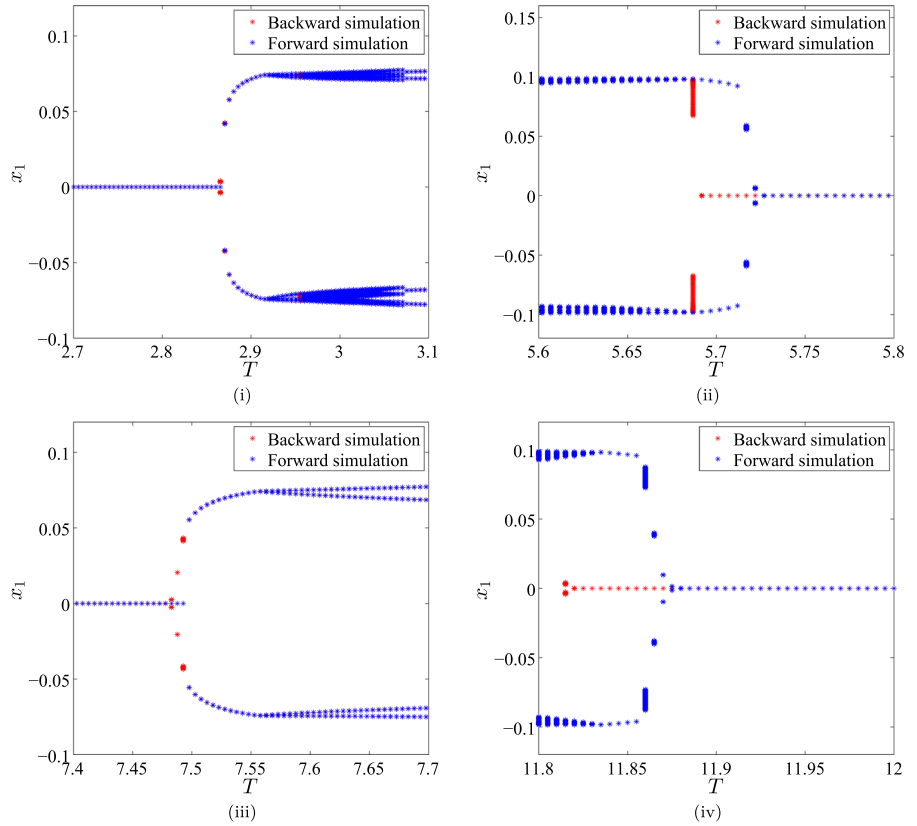
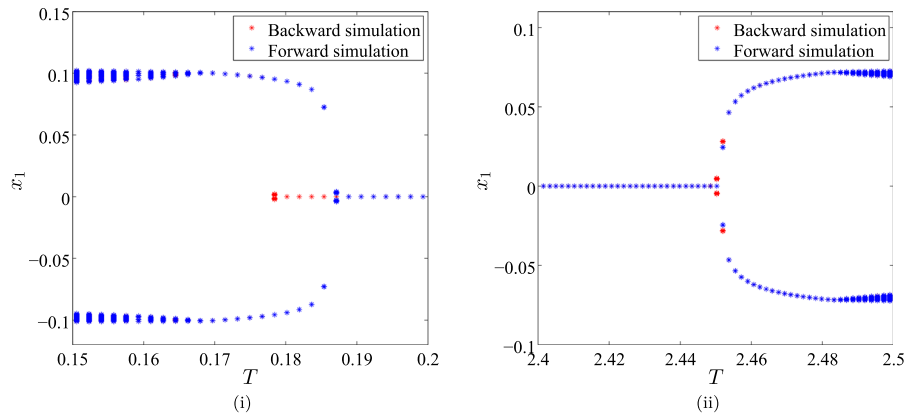


Fig. 12 Zoomed view of Fig. 10ii with different ranges of T . The other parameters are $\sigma_0 = 110$, $\sigma_1 = 1.37$, $\sigma_2 = 0.0823$, $f_s = 0.44$, $f_c = 0.35$, $v_{rv} = 0.1$ $\zeta = 0.2$, $K_0 = 0.5$, $k_i = 0.4$, and $a = 2.5$



and period-2 solutions start appearing in the system. On continuing the numerical simulation with decreasing value of T , we further observe the existence of period-4 and quasi-periodic solutions. Furthermore, after a certain value of T period-1 stick-slip limit cycle again retains stability and undergoes supercritical bifurcation. The representative phase portraits for this

dynamical phenomenon are shown in Fig. 16. From Figs. 11, 12, and 16, we can easily observe that this loss and gain of stability in period-1 solutions through period-doubling bifurcation take place near every Hopf point.

To better understand the appearance of the period-2 solutions, we study the stability of the period-1 solution

Fig. 13 Comparison of bifurcation diagram from numerical simulation and MMS with T as bifurcation parameter (i) supercritical bifurcation, (ii) subcritical bifurcation, (iii) supercritical bifurcation, and (iv) subcritical bifurcation. The other parameters for numerical simulations are $\sigma_0 = 110$, $\sigma_1 = 1.37$, $\sigma_2 = 0.0823$, $f_s = 0.44$, $f_c = 0.35$, $v_{rv} = 0.1$, $\zeta = 0.2$, $K_0 = 0.5$, $k_i = 0.1$, and $a = 2.5$

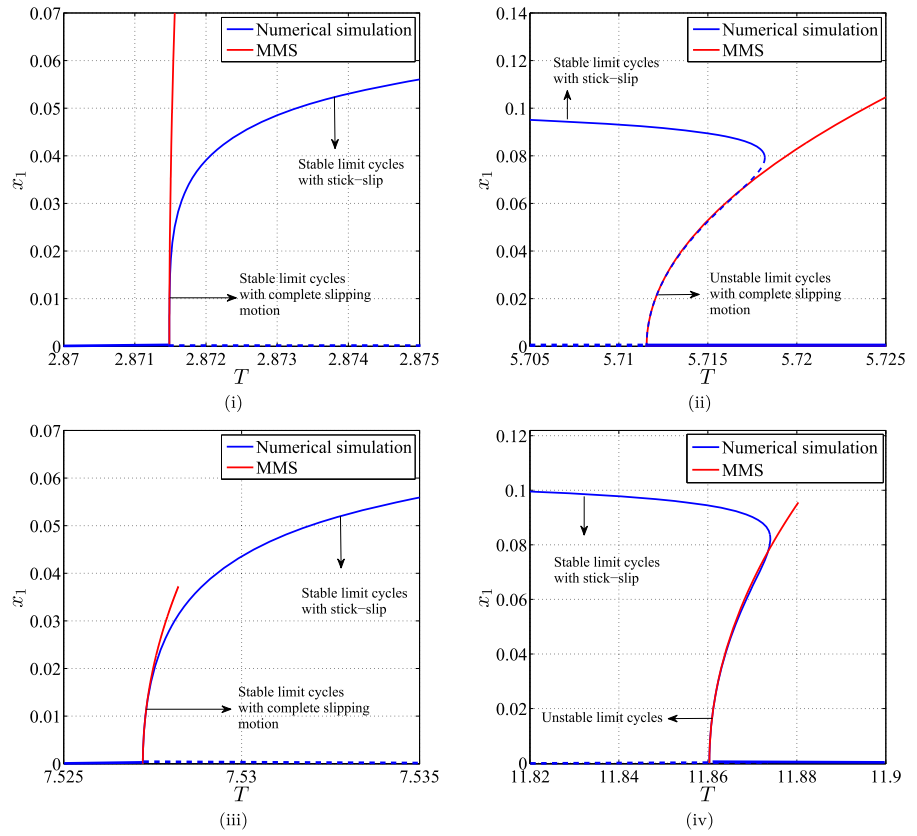
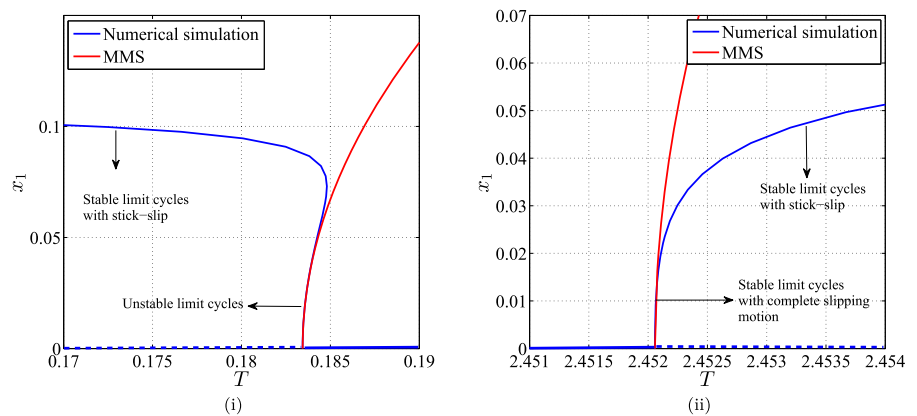


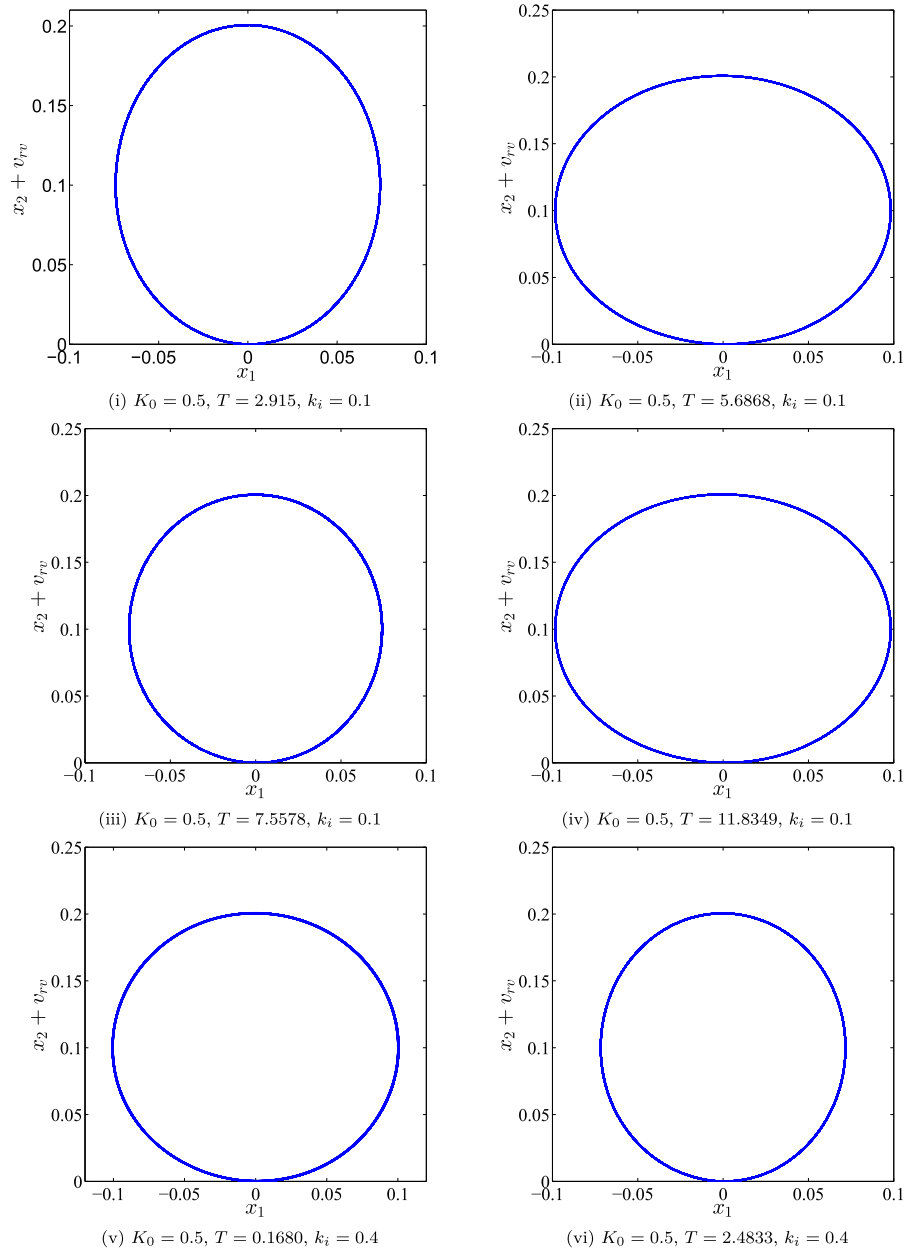
Fig. 14 Comparison of bifurcation diagram from numerical simulation and MMS with T as bifurcation parameter (i) subcritical bifurcation and (ii) supercritical bifurcation. The other parameters for numerical simulations are $\sigma_0 = 110$, $\sigma_1 = 1.37$, $\sigma_2 = 0.0823$, $f_s = 0.44$, $f_c = 0.35$, $v_{rv} = 0.1$, $\zeta = 0.2$, $K_0 = 0.5$, $k_i = 0.4$, and $a = 2.5$



(the stable stick-slip limit cycle preceding the period-2 solutions) using Floquet theory. The movement of the various Floquet multipliers associated with the period-1 solution with decreasing T values around the initiation of the period-2 solution is shown in Fig. 17. We can observe from this figure that the dominant Floquet mul-

tiplier crosses the unit circle at -1 on the real axis and, hence, signifies the loss of stability of period-1 solution through a period-doubling bifurcation [46]. However, on further decreasing the value of T , dominant Floquet multiplier for period-1 solution moves inside the unit circle and becomes stable.

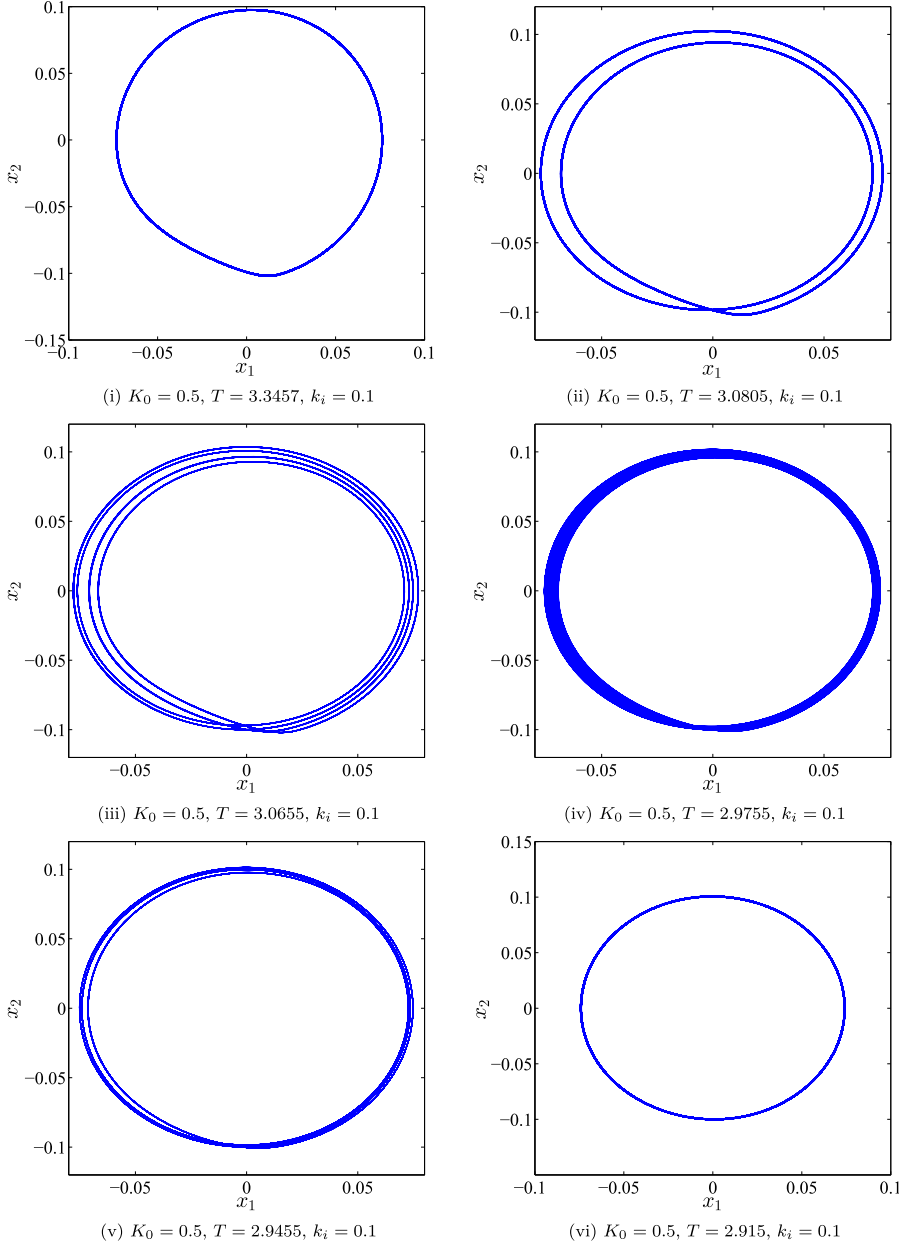
Fig. 15 Phase portraits for the stable limit cycles close to Hopf point with stick-slip motion. The other parameters for numerical simulation are $\sigma_0 = 110$, $\sigma_1 = 1.37$, $\sigma_2 = 0.0823$, $f_s = 0.44$, $f_c = 0.35$, $v_r = 0.1$ $\zeta = 0.2$, $K_0 = 0.5$, and $a = 2.5$



For sake of completeness, we also present the numerical bifurcation for a fixed value of T with varying values of K_0 as shown in Fig. 18 and the representative phase portrait are shown in Fig. 19. We observe that as we change the value of K_0 , steady states lose stability through Hopf bifurcation, and stable stick-slip limit cycles appear in the system. Further, as we increase the value of K_0 , these stable stick-slip limit cycles

become unstable and undergo period-doubling bifurcation. However, after a specific value of K_0 , period-1 stick-slip limit cycles become stable again as in the earlier case. On further exploring the numerical simulations for an increasing value of K_0 , we observe the existence of quasi-periodic and high-amplitude chaotic motions with stick-slip. These high-amplitude chaotic motions further lead to high-amplitude stable limit

Fig. 16 Phase portraits showing the stability of limit cycles with different values of T close to Hopf point (i) period-1 solution, (ii) period-2 solution, (iii) period-4 solution, (iv) quasi-periodic solution, (v) period-2 solution, and (vi) period-1 solution. The other parameters for numerical simulation are $\sigma_0 = 110$, $\sigma_1 = 1.37$, $\sigma_2 = 0.0823$, $f_s = 0.44$, $f_c = 0.35$, $v_r = 0.1$, $\zeta = 0.2$, $K_0 = 0.5$, and $a = 2.5$



cycles in the system as K_0 increases. The observation of the existence of chaotic attractor in the system can be further justified with the help of Lyapunov exponents. As the real part of a Floquet exponent corresponding to a limit cycle represents Lyapunov exponent [47], we use the following relation to determine the Lyapunov exponent

$$\text{L.E.} = \Re \left(\frac{\log(\Phi)}{P} \right), \tag{65}$$

where L.E. represents the Lyapunov exponent, ϕ represents the Floquet multiplier, and P represents the time period of limit cycle. The variation of dominant L.E. with K_0 is shown in Fig. 20. In Fig. 20, zero L.E. corresponds to quasi-periodic motion, while positive value of L.E. corresponds to chaotic attractor. It can be easily observed from Fig. 20 that $K_0 > \approx 1.4$, the dominant L.E. becomes positive, thus confirming the existence of chaotic attractor. The illustrative phase portraits corre-

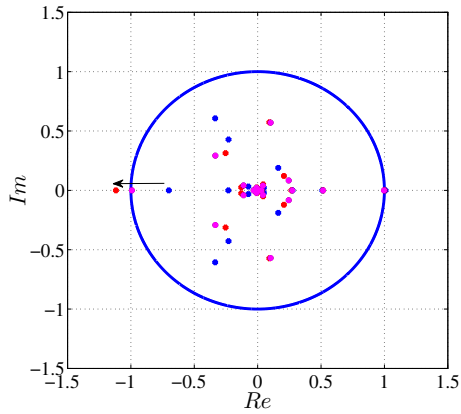


Fig. 17 Floquet multiplier crossing the unit circle through period-doubling bifurcation with blue, magenta, and red colors for earlier, intermediate, and final stage of Floquet multiplier with different values of T ($T = 3.3242$, $T = 3.2491$, and $T = 3.2364$), respectively. (Color figure online)

sponding to the transition in the stability of limit cycles, shown in Fig. 19, also confirm these observations drawn through Fig. 20.

6 Conclusion

This paper presented for the first time the interactions of PID and a proportionate-type time-delayed feedback controller, to control friction-induced vibrations in a precision motion stage. A dynamical friction model, in particular, the LuGre model, was considered for the analysis. It was revealed in earlier works that for the LuGre model the Hopf bifurcation is always subcritical and the nature of Hopf bifurcation can be changed from subcritical to supercritical for a particular choice of control parameters in time-delayed control. However, in contrary to this we observed the existence of multi-

Fig. 18 Numerical bifurcation diagram with K_0 as bifurcation parameter. The zoomed views of (i) for better understanding are shown in (ii), (iii), and (iv). The other parameters are $\sigma_0 = 110$, $\sigma_1 = 1.37$, $\sigma_2 = 0.0823$, $f_s = 0.44$, $f_c = 0.35$, $v_r = 0.1$, $\zeta = 0.2$, $T = 10$, and $a = 2.5$

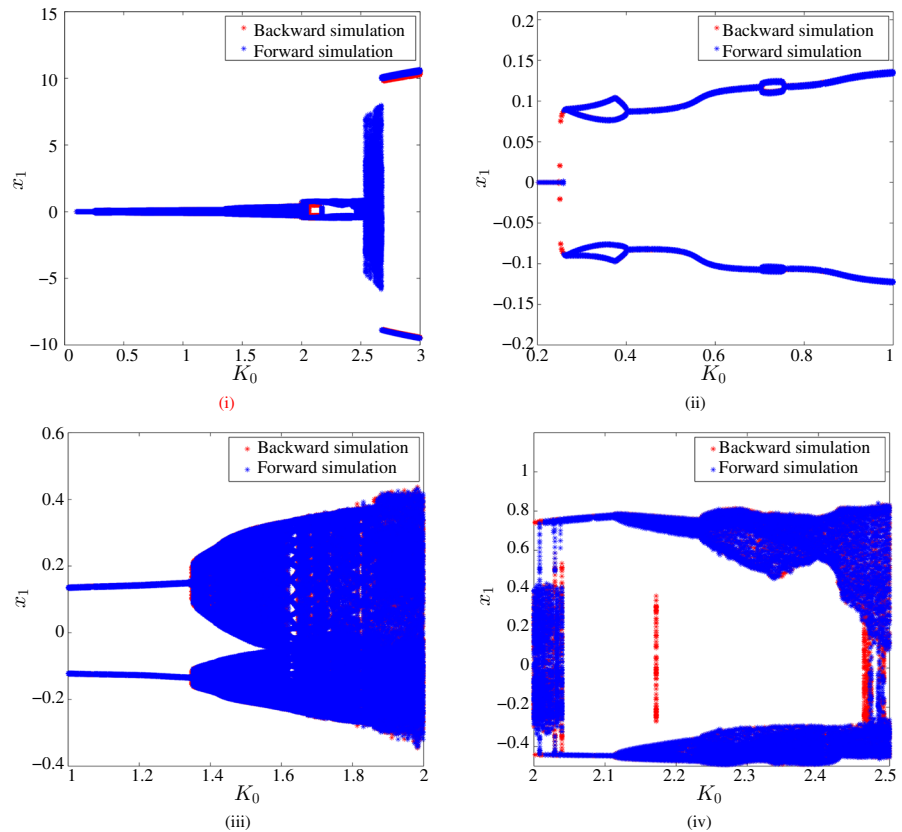
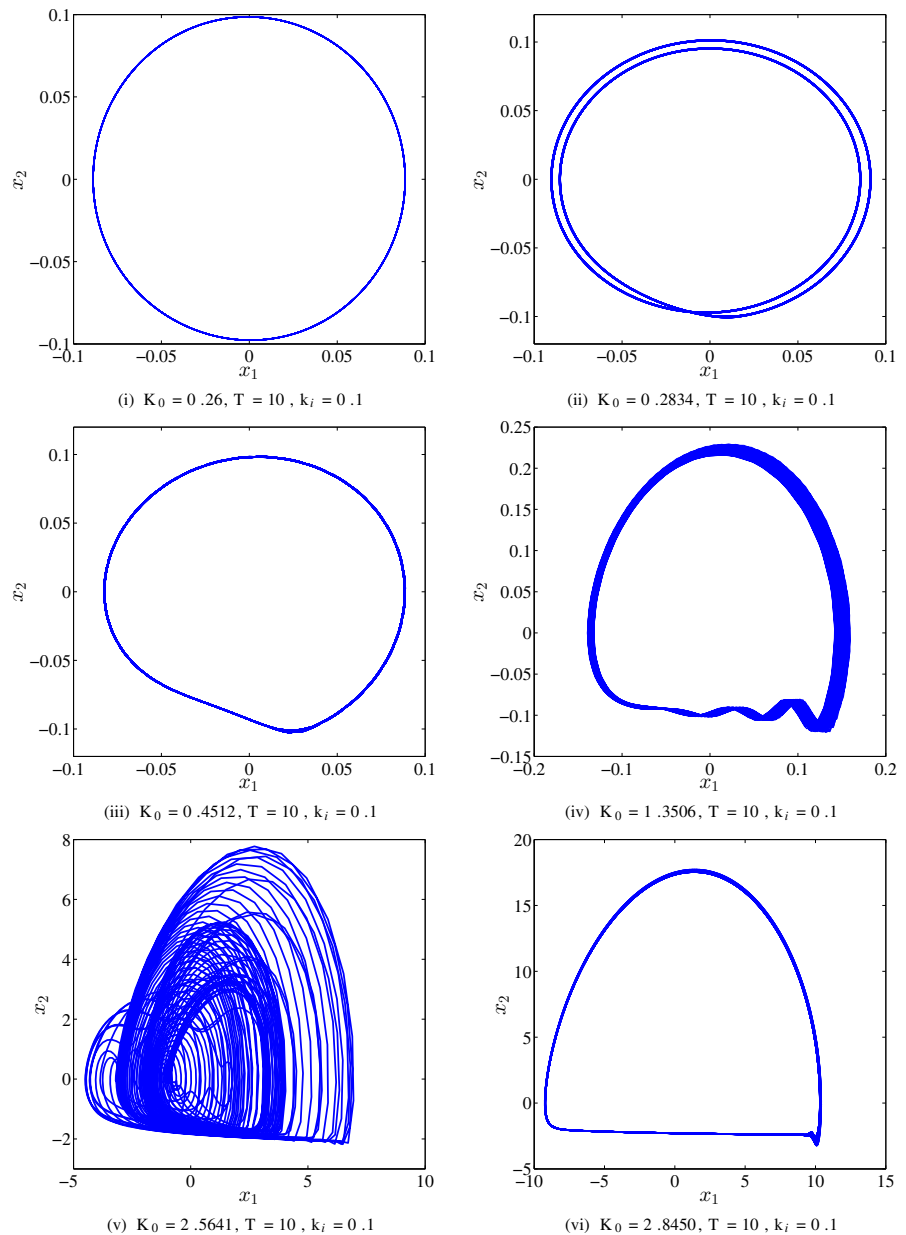


Fig. 19 Phase portraits showing the stability of limit cycles with different values of K_0 (i) period-1 solution, (ii) period-2 solution, (iii) period-1 solution, (iv) quasi-periodic solution, (v) chaotic solution, and (vi) period-1 solution. The other parameters for numerical simulation are $\sigma_0 = 110$, $\sigma_1 = 1.37$, $\sigma_2 = 0.0823$, $f_s = 0.44$, $f_c = 0.35$, $v_r = 0.1$, $\zeta = 0.2$, $K_0 = 0.5$, and $a = 2.5$



ple regions of subcritical and supercritical Hopf bifurcation on the stability lobes for a given value of system parameters. Furthermore, we performed a parametric study on the linear stability boundaries and observed that the stability of the system is very sensitive to integral gain in PID control. There exists a range of values of integral gain for a given value of differential gain

corresponding to multiple stability lobes and, hence, the existence of multiple co-dimension-2 Hopf points. Furthermore, we also noticed that for a given system parameter values, there exists a range of integral gain which ensures the existence of larger stability regime in the system. This observation further implies that larger values of time delay can be used in the time-delayed

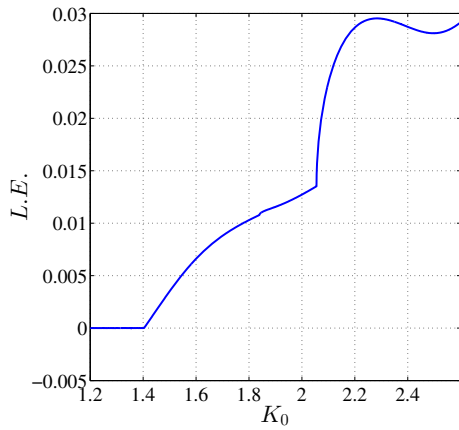


Fig. 20 Variation of dominant Lyapunov exponent with K_0 . The other parameters for numerical simulations are $\sigma_0 = 110$, $\sigma_1 = 1.37$, $\sigma_2 = 0.0823$, $f_s = 0.44$, $f_c = 0.35$, $v_r = 0.1$ $\zeta = 0.2$, $T = 10$, and $a = 2.5$

feedback controller to improve the stability of steady states.

Nonlinear analysis was performed using the method of multiple scales to capture the criticality of Hopf bifurcation on the stability lobes. Accordingly, we obtained different regions of supercritical and sub-critical Hopf bifurcation on the stability curves. The analytical results from the method of multiple scales were further verified with numerical simulation. We observed an excellent match between our analytical findings and numerical simulations. More complicated dynamics in the system have also been observed including period doubling bifurcation, quasi-periodic as well as large-amplitude chaotic motion involving stick-slip and, eventually, large-amplitude stable stick-slip limit cycles.

Having established the use of linear time-delayed feedback controller in PID-controlled motion stages, the use of nonlinear time-delayed feedback controller and the combination of time-delayed feedback with passive isolators have been left for future work.

Acknowledgements This work was funded by National Science Foundation (NSF) Award CMMI #1855390: Towards a Fundamental Understanding of a Simple, Effective and Robust Approach for Mitigating Friction in Nanopositioning Stages.

Compliance with ethical standards

Conflict of interest The authors declare that they have no conflict of interest.

Appendix 1: Expressions used in the linear analysis

$$\begin{aligned}
 n_1 = & -2a_1\omega^6k_i - \omega^{10} - 2v_{rv}^2\sigma_0^2g_0^2\omega^6a_2 \\
 & + v_{rv}^2\sigma_0^2g_0^2\omega^4a_2^2 - 2\omega^6v_{rv}\sigma_0g_0a_1 \\
 & - \omega^6v_{rv}^2\sigma_0^2g_0^2a_1^2 + 2\omega^4v_{rv}^3\sigma_0^3g_0^3a_1 \\
 & + 2k_i^2\omega^2v_{rv}^2\sigma_0^2g_0^2 + 2k_i\omega^4v_{rv}\sigma_0g_0 \\
 & + 2k_i\omega^6v_{rv}\sigma_0g_0 + 2k_iv_{rv}^3\sigma_0^3g_0^3\omega^2 \\
 & + 2k_iv_{rv}^3\sigma_0^3g_0^3\omega^4 + 4\omega^6a_2v_{rv}\sigma_0g_0a_1 \\
 & + \omega^4v_{rv}^2\sigma_0^2g_0^2 - \omega^2v_{rv}^4\sigma_0^4g_0^4 \\
 & + k_i^2v_{rv}^4\sigma_0^4g_0^4 + v_{rv}^2\sigma_0^2g_0^2\omega^8 \\
 & + a_1^2\omega^8 + k_i^2\omega^4 + 2\omega^8a_2 - \omega^6a_2^2 \\
 & - 4\omega^8v_{rv}\sigma_0g_0a_1 - 4\omega^4a_2v_{rv}^2\sigma_0^2g_0^2 \\
 & + 4\omega^6v_{rv}^2\sigma_0^2g_0^2 - 2a_1\omega^4k_iv_{rv}^2\sigma_0^2g_0^2 \\
 & - 2k_i\omega^4v_{rv}\sigma_0g_0a_2 - 2k_iv_{rv}^3\sigma_0^3g_0^3\omega^2a_2
 \end{aligned}$$

$$\begin{aligned}
 d_1 = & \left(\omega^2 + v_{rv}^2\sigma_0^2g_0^2\right) \\
 & \left(\omega^2v_{rv}^2\sigma_0^2g_0^2 + g_0^2\sigma_0^2v_{rv}^2k_i^2\right. \\
 & + 2k_i\omega^2v_{rv}\sigma_0g_0 + 2k_i\omega^4v_{rv}\sigma_0g_0 \\
 & - 2k_i\omega^2v_{rv}\sigma_0g_0a_2 - 2\omega^4v_{rv}\sigma_0g_0a_1 \\
 & - 2\omega^6a_2 + k_i^2\omega^2 + \omega^6a_1^2 + \omega^8 \\
 & \left. + \omega^4a_2^2 - 2a_1\omega^4k_i\right)
 \end{aligned}$$

$$\begin{aligned}
 n_2 = & -2\left(a_1\omega^4 - k_i\omega^2 - k_iv_{rv}^2\sigma_0^2g_0^2\right. \\
 & - v_{rv}\sigma_0g_0\omega^2 - v_{rv}\sigma_0g_0\omega^4 \\
 & \left. + v_{rv}\sigma_0g_0\omega^2a_2\right)\omega \\
 & \left(-v_{rv}^2\sigma_0^2g_0^2 + v_{rv}\sigma_0g_0a_1\omega^2 + \omega^4 - \omega^2a_2\right)
 \end{aligned}$$

$$\begin{aligned}
 d_2 = & \left(\omega^2 + v_{rv}^2\sigma_0^2g_0^2\right) \\
 & \left(\omega^2v_{rv}^2\sigma_0^2g_0^2 + g_0^2\sigma_0^2v_{rv}^2k_i^2\right. \\
 & + 2k_i\omega^2v_{rv}\sigma_0g_0 + 2k_i\omega^4v_{rv}\sigma_0g_0 \\
 & - 2k_i\omega^2v_{rv}\sigma_0g_0a_2 - 2\omega^4v_{rv}\sigma_0g_0a_1 \\
 & - 2\omega^6a_2 + k_i^2\omega^2 + \omega^6a_1^2 + \omega^8 \\
 & \left. + \omega^4a_2^2 - 2a_1\omega^4k_i\right)
 \end{aligned}$$

$$ct = \cos(\omega T) \quad st = \sin(\omega T)$$

$$Re_1 = -\frac{v_{rv}g_1h_0\omega^2}{v_{rv}^2\sigma_0^2g_0^2 + \omega^2}$$

$$Im_1 = \frac{-v_{rv}^2\sigma_0g_0g_1h_0\omega}{v_{rv}^2\sigma_0^2g_0^2 + \omega^2}$$

$$\begin{aligned} \text{Lre}_1 &= \frac{\omega^3 K_0 s t - k_i \omega^2}{-2\omega^2 K_0^2 + 2\omega K_0 s t k_i - k_i^2 + 2\omega^2 K_0^2 c t + 2K_0 c t \omega^2 - 2K_0 \omega^2 - \omega^2} \\ \text{Lim}_1 &= \frac{(\omega^3 - \omega^3 K_0 c t + \omega^3 K_0)}{-2\omega^2 K_0^2 + 2\omega K_0 s t k_i - k_i^2 + 2\omega^2 K_0^2 c t + 2K_0 s t \omega^2 - 2K_0 \omega^2 - \omega^2} \\ \text{Lre}_2 &= \frac{k_i \omega^2 K_0 c t - k_i \omega^2 K_0 - k_i \omega^2}{-2\omega^2 K_0^2 + 2\omega K_0 s t k_i - k_i^2 + 2\omega^2 K_0^2 c t + 2K_0 c t \omega^2 - 2K_0 \omega^2 - \omega^2} \\ \text{Lim}_2 &= \frac{k_i \omega^2 K_0 s t - k_i^2 \omega}{-2\omega^2 K_0^2 + 2\omega K_0 s t k_i - k_i^2 + 2\omega^2 K_0^2 c t + 2K_0 c t \omega^2 - 2K_0 \omega^2 - \omega^2} \\ \text{Lre}_3 &= \frac{-\omega^2 h_2 (\omega K_0 s t v_{rv} \sigma_0 g_0 - k_i v_{rv} \sigma_0 g_0 - K_0 c t \omega^2 + K_0 \omega^2 + \omega^2)}{(v_{rv}^2 \sigma_0^2 g_0^2 + \omega^2) (-2\omega^2 K_0^2 + 2\omega K_0 s t k_i - k_i^2 + 2\omega^2 K_0^2 c t + 2K_0 c t \omega^2 - 2K_0 \omega^2 - \omega^2)} \\ \text{Lim}_3 &= \frac{-\omega^3 h_2 (v_{rv} \sigma_0 g_0 K_0 c t - v_{rv} \sigma_0 g_0 K_0 - v_{rv} \sigma_0 g_0 + \omega K_0 s t - k_i)}{(v_{rv}^2 \sigma_0^2 g_0^2 + \omega^2) (-2\omega^2 K_0^2 + 2\omega K_0 s t k_i - k_i^2 + 2\omega^2 K_0^2 c t + 2K_0 c t \omega^2 - 2K_0 \omega^2 - \omega^2)} \end{aligned}$$

Appendix 2: Expressions used in the nonlinear analysis

$$c t = \cos(\omega T_{cr}) \quad s t = \sin(\omega T_{cr})$$

$$u_{11} = K_{0,cr} T_{cr} c t \quad u_{12} = (\omega - K_{0,cr} T_{cr} s t)$$

$$u_{21} = -\frac{v_{rv} g_1 h_0 \omega^2}{v_{rv}^2 \sigma_0^2 g_0^2 + \omega^2}$$

$$u_{22} = \frac{-v_{rv}^2 \sigma_0 g_0 g_1 h_0 \omega}{v_{rv}^2 \sigma_0^2 g_0^2 + \omega^2}$$

$$\begin{aligned} b_{11} &= -2i\omega^2 e^{2i\omega T_{cr}} \\ &\quad (2i\omega^2 h_0 \sigma_1 h_3 + h_2 \omega h_0 h_3 \\ &\quad - i v_{rv} \sigma_0 g_0 \sigma_1 h_4 Re_1 + \sigma_1 h_4 Im_1 v_{rv} \sigma_0 g_0 \\ &\quad + h_0 \sigma_1 h_3 \omega v_{rv} \sigma_0 g_0 + 2i\omega \sigma_1 h_4 Im_1 \\ &\quad - i h_4 Re_1 h_2 + h_2 h_4 Im_1 + 2\sigma_1 h_4 \omega Re_1) / \\ &\quad (e^{2i\omega T_{cr}} k_i v_{rv} \sigma_0 g_0 + 2i e^{2i\omega T_{cr}} k_i \omega \\ &\quad - 4\omega^2 h_1 e^{2i\omega T_{cr}} v_{rv} \sigma_0 g_0 - 8i\omega^3 h_1 e^{2i\omega T_{cr}} \\ &\quad - 2i\omega K_0 v_{rv} \sigma_0 g_0 + 4K_0 \omega^2 + 2i\omega e^{2i\omega T_{cr}} v_{rv} \sigma_0 g_0 \\ &\quad - 4\omega^2 e^{2i\omega T_{cr}} - 8i\omega^3 e^{2i\omega T_{cr}} v_{rv} \sigma_0 g_0 \\ &\quad + 16\omega^4 e^{2i\omega T_{cr}} + 4e^{i\omega T_{cr}^2} h_2 v_{rv} g_1 h_0 \omega^2 \\ &\quad + 2i\omega K_0 e^{2i\omega T_{cr}} v_{rv} \sigma_0 g_0 - 4\omega^2 K_0 e^{2i\omega T_{cr}}) \end{aligned}$$

$$\begin{aligned} b_{12} &= 4\omega^3 e^{2i\omega T_{cr}} \\ &\quad (2i\omega^2 h_0 \sigma_1 h_3 + h_2 \omega h_0 h_3 \\ &\quad - i v_{rv} \sigma_0 g_0 \sigma_1 h_4 Re_1 + \sigma_1 h_4 Im_1 v_{rv} \sigma_0 g_0 \\ &\quad + h_0 \sigma_1 h_3 \omega v_{rv} \sigma_0 g_0 + 2i\omega \sigma_1 h_4 Im_1 \\ &\quad - i h_4 Re_1 h_2 + h_2 h_4 Im_1 + 2\sigma_1 h_4 \omega Re_1) / \\ &\quad (e^{2i\omega T_{cr}} k_i v_{rv} \sigma_0 g_0 + 2i e^{2i\omega T_{cr}} k_i \omega \end{aligned}$$

$$\begin{aligned} &\quad - 4\omega^2 h_1 e^{2i\omega T_{cr}} v_{rv} \sigma_0 g_0 - 8i\omega^3 h_1 e^{2i\omega T_{cr}} \\ &\quad - 2i\omega K_0 v_{rv} \sigma_0 g_0 + 4K_0 \omega^2 \\ &\quad + 2i\omega e^{2i\omega T_{cr}} v_{rv} \sigma_0 g_0 - 4\omega^2 e^{2i\omega T_{cr}} \\ &\quad - 8i\omega^3 e^{2i\omega T_{cr}} v_{rv} \sigma_0 g_0 + 16\omega^4 e^{2i\omega T_{cr}} \\ &\quad + 4e^{i\omega T_{cr}^2} h_2 v_{rv} g_1 h_0 \omega^2 \\ &\quad + 2i\omega K_0 e^{2i\omega T_{cr}} v_{rv} \sigma_0 g_0 - 4\omega^2 K_0 e^{2i\omega T_{cr}}) \\ b_{13} &= -\omega e^{2i\omega T_{cr}} \\ &\quad (2i\omega^2 h_0 \sigma_1 h_3 + h_2 \omega h_0 h_3 \\ &\quad - i v_{rv} \sigma_0 g_0 \sigma_1 h_4 Re_1 + \sigma_1 h_4 Im_1 v_{rv} \sigma_0 g_0 \\ &\quad + h_0 \sigma_1 h_3 \omega v_{rv} \sigma_0 g_0 + 2i\omega \sigma_1 h_4 Im_1 \\ &\quad - i h_4 Re_1 h_2 + h_2 h_4 Im_1 + 2\sigma_1 h_4 \omega Re_1) / \\ &\quad (e^{2i\omega T_{cr}} k_i v_{rv} \sigma_0 g_0 + 2i e^{2i\omega T_{cr}} k_i \omega \\ &\quad - 4\omega^2 h_1 e^{2i\omega T_{cr}} v_{rv} \sigma_0 g_0 - 8i\omega^3 h_1 e^{2i\omega T_{cr}} \\ &\quad - 2i\omega K_0 v_{rv} \sigma_0 g_0 + 4K_0 \omega^2 \\ &\quad + 2i\omega e^{2i\omega T_{cr}} v_{rv} \sigma_0 g_0 - 4\omega^2 e^{2i\omega T_{cr}} \\ &\quad - 8i\omega^3 e^{2i\omega T_{cr}} v_{rv} \sigma_0 g_0 + 16\omega^4 e^{2i\omega T_{cr}} \\ &\quad + 4e^{2i\omega T_{cr}} h_2 v_{rv} g_1 h_0 \omega^2 \\ &\quad + 2i\omega K_0 e^{2i\omega T_{cr}} v_{rv} \sigma_0 g_0 \\ &\quad - 4\omega^2 K_0 e^{i\omega T_{cr}}) \\ b_{14} &= (-4h_0^2 \sigma_1 h_3 \omega^3 e^{2i\omega T_{cr}} v_{rv} g_1 \\ &\quad - 4\sigma_1 h_4 \omega^2 Im_1 e^{2i\omega T_{cr}} v_{rv} g_1 h_0 \\ &\quad + 2i\omega^2 K_0 e^{2i\omega T_{cr}} h_0 h_3 - 4\omega^3 h_1 e^{2i\omega T_{cr}} h_0 h_3 \\ &\quad - 4\omega^2 h_1 e^{2i\omega T_{cr}} h_4 Im_1 - 8i\omega^3 e^{2i\omega T_{cr}} h_4 Im_1 \\ &\quad - 8i\omega^4 e^{2i\omega T_{cr}} h_0 h_3 + e^{2i\omega T_{cr}} k_i h_0 h_3 \omega \\ &\quad + e^{2i\omega T_{cr}} k_i h_4 Im_1 + 2\omega e^{i\omega T_{cr}} h_4 Re_1 \end{aligned}$$

$$\begin{aligned}
 & -ie^{2i\omega T_{cr}} k_i h_4 Re_1 + 4i\omega^2 h_1 e^{2i\omega T_{cr}} h_4 Re_1 \\
 & -2\omega K_0 h_4 Re_1 + 2i\omega K_0 e d^2 h_4 Im_1 \\
 & + 2i\omega e^{2i\omega T_{cr}} h_4 Im_1 + 2\omega K_0 e^{2i\omega T_{cr}} h_4 Re_1 \\
 & -2i\omega^2 K_0 h_0 h_3 - 2i\omega K_0 h_4 Im_1 \\
 & -8\omega^3 e^{2i\omega T_{cr}} h_4 Re_1 \\
 & + 4i\sigma_1 h_4 \omega^2 Re_1 e^{2i\omega T_{cr}} v_{rv} g_1 h_0 \\
 & + 2i\omega^2 e^{i\omega T_{cr}} h_0 h_3 \Big) \omega / \\
 & \left(e^{2i\omega T_{cr}} k_i v_{rv} \sigma_0 g_0 + 2ie^{2i\omega T_{cr}} k_i \omega \right. \\
 & - 4\omega^2 h_1 e^{2i\omega T_{cr}} v_{rv} \sigma_0 g_0 \\
 & - 8i\omega^3 h_1 e^{2i\omega T_{cr}} - 2i\omega K_0 v_{rv} \sigma_0 g_0 + 4K_0 \omega^2 \\
 & + 2i\omega e^{2i\omega T_{cr}} v_{rv} \sigma_0 g_0 - 4\omega^2 e^{2i\omega T_{cr}} \\
 & - 8i\omega^3 e^{i\omega T_{cr}} v_{rv} \sigma_0 g_0 + 16\omega^4 e^{i\omega T_{cr}} \\
 & + 4e^{2i\omega T_{cr}} h_2 v_{rv} g_1 h_0 \omega^2 \\
 & \left. + 2i\omega K_0 e^{2i\omega T_{cr}} v_{rv} \sigma_0 g_0 - 4\omega^2 K_0 e^{2i\omega T_{cr}} \right)
 \end{aligned}$$

$$b_{31} = b_{32} = 0,$$

$$b_{33} = 2 \frac{\omega (h_2 h_4 Im_1 + h_2 \omega h_0 h_3 + \sigma_1 h_4 Im_1 v_{rv} \sigma_0 g_0 + h_0 \sigma_1 h_3 \omega v_{rv} \sigma_0 g_0)}{k_i v_{rv} \sigma_0 g_0},$$

$$b_{34} = -2 \frac{\omega (h_4 Im_1 + h_0 h_3 \omega)}{v_{rv} \sigma_0 g_0}$$

$$v_{11} = i\omega + e^{-i\omega T_{cr}} K_0 T_{cr} \quad v_{21} = Re_1 + iIm_1$$

$$\begin{aligned}
 v_{12} = & i\sigma_1 h_4 A_1 (T_2)^2 b_{12} A_2 (T_2) Im_1 - 3i\sigma_1 h_5 \omega^3 A_1 (T_2)^2 A_2 (T_2) \\
 & + i\sigma_1 h_4 \omega A_2 (T_2) A_1 (T_2)^2 b_{14} + 2ih_0 \sigma_1 h_3 \omega A_2 (T_2) A_1 (T_2)^2 b_{12} \\
 & - \sigma_1 \sigma_0 h_3 \omega^2 A_1 (T_2)^2 A_2 (T_2) Re_1 - \sigma_1 h_4 A_1 (T_2)^2 b_{12} A_2 (T_2) Re_1 \\
 & - i\sigma_1 h_4 \omega A_1 (T_2)^2 A_2 (T_2) b_{34} - 3i\sigma_1 \sigma_0 h_3 \omega^2 A_1 (T_2)^2 A_2 (T_2) Im_1 \\
 & + ie^{-i\omega T_{cr}} K_0 k_1 A_1 (T_2) \omega
 \end{aligned}$$

$$\begin{aligned}
 v_{22} = & -2ih_0 h_3 \omega A_2 (T_2) A_1 (T_2)^2 b_{12} - ih_4 \omega A_2 (T_2) A_1 (T_2)^2 b_{14} \\
 & + ih_4 \omega A_1 (T_2)^2 A_2 (T_2) b_{34} + \sigma_0 h_3 \omega^2 A_1 (T_2)^2 A_2 (T_2) Re_1 \\
 & + h_4 A_1 (T_2)^2 b_{12} A_2 (T_2) Re_1 - ih_4 A_1 (T_2)^2 b_{12} A_2 (T_2) Im_1 \\
 & + 3ih_5 \omega^3 A_1 (T_2)^2 A_2 (T_2) + 3i\sigma_0 h_3 \omega^2 A_1 (T_2)^2 A_2 (T_2) Im_1
 \end{aligned}$$

References

1. Kim, W., Trumper, D.L.: High-precision magnetic levitation stage for photolithography. *Precis. Eng.* **22**(2), 66–77 (1998)
2. Kim, W.J., Verma, S., Shakir, H.: Design and precision construction of novel magnetic-levitation-based multi-axis nanoscale positioning systems. *Precis. Eng.* **31**(4), 337–350 (2007)
3. Salapaka, S.M., Salapaka, M.V.: Scanning probe microscopy. *IEEE Control Syst. Mag.* **28**(2), 65–83 (2008)
4. Sebastian, A., Pantazi, A., Moheimani, S.O.R., Pozidis, H., Eleftheriou, E.: Achieving subnanometer precision in a mems-based storage device during self-servo write process. *IEEE Trans. Nanotechnol.* **7**(5), 586–595 (2008)

5. Fleming, A.J., Leang, K.K.: *Design, Modeling and Control of Nanopositioning Systems*. Springer, Berlin (2014)
6. Butler, H.: Position control in lithographic equipment. *IEEE Control Syst. Mag.* **31**(5), 28–47 (2011)
7. Altintas, Y., Verl, A., Brecher, C., Uriarte, L., Pritschow, G.: Machine tool feed drives. *CIRP Ann* **60**(2), 779–796 (2011)
8. Al-Bender, F., Swevers, J.: Characterization of friction force dynamics. *IEEE Control Syst. Mag.* **28**(6), 64–81 (2008)
9. Marques, F., Flores, P., Claro, J.C.P., Lankarani, H.M.: A survey and comparison of several friction force models for dynamic analysis of multibody mechanical systems. *Non-linear Dyn.* **86**(3), 1407–1443 (2016)
10. Futami, S., Furutani, A., Yoshida, S.: Nanometer positioning and its micro-dynamics. *Nanotechnology* **1**(1), 31 (1990)
11. Armstrong-Hélouvy, B., Dupont, P., Wit, C.C.D.: A survey of models, analysis tools and compensation methods for the control of machines with friction. *Automatica* **30**(7), 1083–1138 (1994)
12. Hensen, R.H.A., Van de Molengraft, M.J.G., Steinbuch, M.: Friction induced hunting limit cycles: a comparison between the lugre and switch friction model. *Automatica* **39**(12), 2131–2137 (2003)
13. Maeda, Y., Iwasaki, M.: Rolling friction model-based analyses and compensation for slow settling response in precise positioning. *IEEE Trans. Ind. Electron.* **60**(12), 5841–5853 (2012)
14. Dong, X., Yoon, D., Okwudire, C.E.: A novel approach for mitigating the effects of pre-rolling/pre-sliding friction on the settling time of rolling bearing nanopositioning stages using high frequency vibration. *Precis. Eng.* **47**, 375–388 (2017)
15. Kim, M.-S., Kim, J.-H.: Design of a gain scheduled pid controller for the precision stage in lithography. *Int. J. Precis. Eng. Manuf.* **12**(6), 993–1000 (2011)
16. Liu, J.-Y., Yin, W.-S., Zhu, Y.: Application of adaptive fuzzy pid controller to nano-scale precision motion stage system. *Control Eng. China* **18**(2), 254–257 (2011)
17. Dejjima, S., Gao, W., Katakura, K., Kiyono, S., Tomita, Y.: Dynamic modeling, controller design and experimental validation of a planar motion stage for precision positioning. *Precis. Eng.* **29**(3), 263–271 (2005)
18. Yao, J., Deng, W., Jiao, Z.: Adaptive control of hydraulic actuators with lugre model-based friction compensation. *IEEE Trans. Ind. Electron.* **62**(10), 6469–6477 (2015)
19. Wang, X., Wang, S.: High performance adaptive control of mechanical servo system with lugre friction model: identification and compensation. *J. Dyn. Syst. Meas. Control* **134**(1), 011021 (2012)
20. Conceição, A.G.S., Dórea, C.E.T., Martinez, L., de Pieri, E.R., et al.: Design and implementation of model-predictive control with friction compensation on an omnidirectional mobile robot. *IEEE/ASME Trans. Mechatron.* **19**(2), 467–476 (2013)
21. Dong, X., Liu, X., Yoon, D., Okwudire, C.E.: Simple and robust feedforward compensation of quadrant glitches using a compliant joint. *CIRP Ann.* **66**(1), 353–356 (2017)
22. Dong, X., Okwudire, C.E.: An experimental investigation of the effects of the compliant joint method on feedback compensation of pre-sliding/pre-rolling friction. *Precis. Eng.* **54**, 81–90 (2018)

23. Maccari, A.: Vibration control for the primary resonance of a cantilever beam by a time delay state feedback. *J. Sound Vib.* **259**(2), 241–251 (2003)
24. Atay, F.M.: Van der pol's oscillator under delayed feedback. *J. Sound Vib.* **218**(2), 333–339 (1998)
25. Maccari, A.: Vibration control for the primary resonance of the van der pol oscillator by a time delay state feedback. *Int. J. Non-Linear Mech.* **38**(1), 123–131 (2003)
26. Haiyan, H., Dowell, E.H., Virgin, L.N.: Resonances of a harmonically forced duffing oscillator with time delay state feedback. *Nonlinear Dyn.* **15**(4), 311–327 (1998)
27. Qian, C., Tang, J.: A time delay control for a nonlinear dynamic beam under moving load. *J. Sound Vib.* **309**(1–2), 1–8 (2008)
28. Das, J.K., Mallik, A.K.: Control of friction driven oscillation by time-delayed state feedback. *J. Sound Vib.* **297**(3–5), 578–594 (2006)
29. Chatterjee, S.: Time-delayed feedback control of friction-induced instability. *Int. J. Non-Linear Mech.* **42**(9), 1127–1143 (2007)
30. Neubauer, M., Neuber, C.-C., Popp, K.: Control of stick-slip vibrations. In: *IUTAM Symposium on Vibration Control of Nonlinear Mechanisms and Structures*, pp. 223–232. Springer (2005)
31. Lee, J.H.: Model predictive control: review of the three decades of development. *Int. J. Control Autom. Syst.* **9**(3), 415 (2011)
32. Krsti, M., Kanellakopoulos, I., Petar, V.: *Nonlinear and Adaptive Control Design*. Wiley, New York (1995)
33. Dong, X., Okwudire, C., Wang, J., Barry, O.: On the friction isolator for precision motion control and its dynamics. In: *ASME 2019 International Design Engineering Technical Conferences and Computers and Information in Engineering Conference*. American Society of Mechanical Engineers Digital Collection (2019)
34. Wang, J., Dong, X., Barry, O.R., Okwudire, C.: Dynamical analysis of friction induced vibration in a precision motion stage with a friction isolator. *arXiv preprint arXiv:1910.03212* (2019)
35. De Wit, C.C., Olsson, H., Astrom, K.J., Lischinsky, P.: A new model for control of systems with friction. *IEEE Trans. Autom. Control* **40**(3), 419–425 (1995)
36. Chatterjee, S.: Non-linear control of friction-induced self-excited vibration. *Int. J. Non-Linear Mech.* **42**(3), 459–469 (2007)
37. Johanaström, K., Canudas-De-Wit, C.: Revisiting the lugre friction model. *IEEE Control Syst. Mag.* **28**(6), 101–114 (2008)
38. Pennestrì, E., Rossi, V., Salvini, P., Valentini, P.P.: Review and comparison of dry friction force models. *Nonlinear Dyn.* **83**(4), 1785–1801 (2016)
39. Marques, F., Flores, P., Claro, J.C.P., Lankarani, H.M.: Modeling and analysis of friction including rolling effects in multibody dynamics: a review. *Multibody Syst. Dyn.* **45**(2), 223–244 (2019)
40. Saha, A., Wahi, P.: An analytical study of time-delayed control of friction-induced vibrations in a system with a dynamic friction model. *Int. J. Non-Linear Mech.* **63**, 60–70 (2014)
41. Saha, A.: Analysis and control of friction-induced vibrations by time-delayed feedback. PhD thesis, Indian Institute of Technology, Kanpur, India (2013)
42. Balachandran, B., Nayfeh, A.H.: Cyclic motions near a hopf bifurcation of a four-dimensional system. *Nonlinear Dyn.* **3**(1), 19–39 (1992)
43. Wahi, P., Chatterjee, A.: Galerkin projections for delay differential equations. In: *ASME 2003 International Design Engineering Technical Conferences and Computers and Information in Engineering Conference*, pp. 2211–2220. American Society of Mechanical Engineers (2003)
44. Gupta, S.K., Wahi, P.: Global axial-torsional dynamics during rotary drilling. *J. Sound Vib.* **375**, 332–352 (2016)
45. Wahi, P., Chatterjee, A.: Self-interrupted regenerative metal cutting in turning. *Int. J. Non-Linear Mech.* **43**(2), 111–123 (2008)
46. Scott, S.K.: *Chemical Chaos*. International Series of Monographs on Chemistry. Clarendon Press, Oxford (1993)
47. Anishchenko, V.S., Vadivasova, T.E., Strelkova, G.I.: *Deterministic Nonlinear Systems: A Short Course*. Springer Series in Synergetics. Springer, Berlin (2014)

Publisher's Note Springer Nature remains neutral with regard to jurisdictional claims in published maps and institutional affiliations.